A new salinity-based model for Cryogenian Mn-carbonate deposits

Wei Wei [a,b,c,d], Wenchao Yu [a,*], Yuansheng Du [a], Thomas J. Algeo [a,b,c], Zhiquan Li [d],
Meng Cheng [b], Ping Wang [e], Jingyu Zhang [f], Leslie J. Robbins [g], Kurt Konhauser [d]

[a] State Key Laboratory of Geological Processes and Mineral Resources, School of Earth Sciences, China University of Geosciences, Wuhan 430074, China
[b] State Key Laboratory of Biogeology and Environmental Geology, China University of Geosciences, Wuhan 430074, China
[c] Department of Geosciences, University of Cincinnati, Cincinnati, OH 45221, USA
[d] Department of Earth and Atmospheric Sciences, University of Alberta, Edmonton, AB T6G 2E3, Canada
[e] Institute of Resources and Environment, Henan Polytechnic University, Jiaozuo, 454003, China
[f] School of Earth Resources, China University of Geosciences, Wuhan 430074, China
[g] Department of Geology, University of Regina, Regina, SK S4S 0A2, Canada

ARTICLE INFO

ABSTRACT

The genesis of manganese (Mn)-carbonate deposits in the Cryogenian Datangpo Formation (~662.9–654.5 Ma), Nanhua Basin, South China remains controversial. Here, we combine new proxy data (B/Ga) for watermass salinity with existing data (major- and trace-element concentrations, bulk-rock Sr and Nd isotopes, pyrite sulfur isotopes, and organic and inorganic carbon isotopes) for redox and other environmental parameters to gain new insights into the conditions under which these deposits formed. Our analysis focuses on the Mn-carbonates of the 1st Member of the Datangpo Formation, which were deposited at the termination of the Sturtian Ice Age, with an emphasis on understanding their environment of formation, Mn sources, and microbial processes. Close relationships between Mn content and salinity (B/Ga), redox (C_{org}/P, Cu_{EF}), and carbon-cycle ($\delta^{13}C_{carb}$, $\delta^{13}C_{org}$) proxies reveal a dominant role of salinity in the development of these Mn-rich deposits. These relationships document Mn accumulation in a watermass that fluctuated between brackish, euxinic conditions (Mn-shale beds) and saline, ferruginous conditions (Mn-carbonate beds). Significant correlations between Mn content and hydrothermal proxies (Eu/Eu*, $^{87}Sr/^{86}Sr$ and $\varepsilon Nd(i)$), as well as covariation of $(^{87}Sr/^{86}Sr)_i$ vs $\varepsilon Nd(i)$ and Fe/Ti vs Al/(Al + Fe + Mn), suggest that Mn was sourced mainly from hydrothermal vents in the deep Nanhua Basin. Episodic hydrothermal activity also provided nutrients that boosted primary productivity and organic matter accumulation rates in the form of mineralized biomats. Partial oxidation of the organic carbon coupled to dissimilatory Mn(IV) reduction promoted Mn(II)-carbonate formation in conjunction with high levels of glacially generated alkalinity. A similar confluence of factors (i.e., high background alkalinity, hydrothermal inputs of Mn and nutrients, and microbial activity) may have played a role in the formation of large-scale Mn-ore deposits during other geologic epochs.

1. Introduction

The Cryogenian Period (~720–635 Ma) was characterized by deposition of massive manganese (Mn) deposits and the reappearance of banded iron formations (BIF) in South China and around the world (Maynard, 2010; Xu et al., 2019; Freitas et al., 2021). In the Nanhua Basin of South China, economic quantities of Mn-carbonates accumulated in the 1st Member of the Datangpo Formation during the interglacial interval between the Sturtian (~720–660 Ma) and Marinoan (~654–635 Ma) ice ages (Shields-Zhou et al., 2012; Rooney et al., 2015)

[note: our designation of these glacial events as "ice ages" follows Yu et al. (2020)]. Other Mn-carbonates that were deposited around this time include those of the Penganga Group at Adilabad, India (Gutzmer and Beukes, 1998; Maynard and Kuleshov, 2017), and the massive, post-Marinoan Mn and Fe deposits of the Santa Cruz Formation of the Urucum District of Brazil (Urban et al., 1992; Freitas et al., 2021). These deposits have been inferred to share certain features, including hydrothermal inputs, fluctuating environmental redox conditions, and microbially mediated carbonate precipitation. However, specific aspects of their formation remain poorly resolved, especially regarding

watermass salinity and its relationship to redox and productivity conditions, as well as the sources of manganese and alkalinity for Mn(II)-carbonate formation (herein simply referred to as Mn-carbonates).

Several environmental features of the post-Sturtian Nanhua Basin and their relationship to Mn-ore formation have been the subject of considerable study. For instance, Mn-carbonate precipitation has previously been linked to episodic oxygenation events (Yu et al., 2016; Xiao et al., 2017, 2019), although more recent Fe-speciation studies have inferred uniformly anoxic conditions, with black shale and Mn-carbonate intervals representing euxinic and ferruginous conditions, respectively (Ye et al., 2018; Ma et al., 2019; Cheng et al., 2020; Tan et al., 2021). It has also been suggested that primary productivity was generally high owing to rising sea levels and that there was a greater nutrient supply from the open ocean (Li et al., 2012; Ai et al., 2021). In turn, this would have led to the intense decomposition of organic matter, which may have contributed alkalinity (HCO_3^- and CO_3^{2-}) essential for Mn-carbonate precipitation (Polgári et al., 2012; Häusler et al., 2018). While geochemical signatures suggest that hydrothermal activity was the main source of Mn^{2+} within the Nanhua Basin (Yu et al., 2016), intense weathering of fine glacial debris (Wang et al., 2019) may represent another potential source of both Mn^{2+} and alkalinity (Ma et al., 2019; Yu et al., 2020, 2022). What has been lacking in virtually all these studies, however, is consideration of potential fluctuations in watermass salinity and how they were related to variations in redox and productivity, and ultimately to the sources of manganese and alkalinity necessary for the formation of Mn-carbonates.

It has been assumed, either implicitly or explicitly, by most previous studies that the Datangpo Formation was deposited under fully marine conditions (e.g., Wang and Li, 2003; Zhang et al., 2015). The first study to examine watermass salinity variation inferred highly dynamic conditions, with fluctuations ranging from low-brackish to fully marine salinities (Cheng et al., 2021). The only other paleosalinity study to date (Yu et al., 2022) demonstrated that the Nanhua Basin water column was salinity-stratified, with a reduced-salinity surface layer overlying a fully marine deep layer. These findings suggest that secular variation in freshwater runoff and/or watermass exchange with the open ocean had the potential to exert a strong influence on both salinity and other environmental properties that controlled Mn-ore formation in the post-Sturtian Nanhua Basin. Paleosalinity analysis has the potential to clarify relationships between salinity, redox, productivity, and chemical fluxes and, thus, to yield significant new insights into the genesis of Datangpo Formation Mn-ore deposits (Gilleaudeau et al., 2021; Song et al., 2021).

Here, we make use of three elemental ratios (i.e., B/Ga, Sr/Ba, and S/TOC) that were recently proposed as useful proxies for watermass salinity in ancient shale and mudstone units, based on calibration of salinity facies thresholds in modern sediments deposited in waters of known salinity (Wei and Algeo, 2020). These salinity proxies have already yielded valuable insights regarding paleoenvironmental conditions in shale depositional systems covering a range of ages (e.g., Remírez and Algeo, 2020; Gilleaudeau et al., 2021; Song et al., 2021; Wei et al., 2022). In the present study, we evaluate salinity proxy data for the 1st Member of the Datangpo Formation along with petrographic and geochemical data (i.e., major and trace elements, $^{87}Sr/^{86}Sr$, $^{143}Nd/^{144}Nd$, $\delta^{13}C_{org}$, $\delta^{13}C_{carb}$, $\delta^{34}S_{CAS}$, and $\delta^{34}S_{py}$). Although we draw some petrographic and geochemical data from Yu et al., (2019, 2022), those two studies were focused respectively on the microbial metallogenetic mechanism and the alkalinity source of the Datangpo Mn-carbonate deposits. The present study was undertaken with completely different aims, specifically: (1) evaluating the relationships between salinity and other environmental parameters (e.g., redox conditions, hydrothermal inputs, and microbial activity) in the Cryogenian Nanhua Basin; (2) better constraining the Mn source for Datangpo Formation Mn-carbonates; and (3) developing a revised, salinity-based model of Mn-carbonate formation in the post-Sturtian Nanhua Basin. Our findings are likely to have application to other penecontemporaneous Mn deposits globally.

2. Geological setting

The supercontinent Rodinia was assembled between 1300 and 900 Ma (Fig. 1A; Li et al., 2008) and subsequently broke up at ~ 750 Ma (Hoffman and Schrag, 2002, Goddéris et al., 2003, 2007). Its breakup yielded multiple cratons, including the South China, North China, and Tarim cratons located in present-day China. These resultant cratons were mostly located in the paleo-tropics and subjected to high rates of erosion and weathering (Hoffman and Schrag, 2002, Goddéris et al., 2003, 2007; Merdith et al., 2021). Strong drawdown of atmospheric CO_2 levels associated with weathering of mafic–ultramafic rocks and increased organic matter (OM) burial linked to expansion of the early metazoan biosphere (Love et al., 2009; Feulner et al., 2015; Slater and Bohlin, 2022) triggered global glaciations (or 'Snowball Earth' events) that define the Cryogenian Period, i.e., the Sturtian (~720–660 Ma) and Marinoan (~654–635 Ma) ice ages (Ridgwell et al., 2003; Shields-Zhou et al., 2012; Rooney et al., 2015; Cox et al., 2016; Hoffman et al., 2017; Pu et al., 2022). These glacial episodes caused major changes in the chemistry of Earth's oceans, leading to widespread formation of manganese (Mn) ore deposits and banded iron formations (BIF) (e.g., Urban et al., 1992; Gutzmer and Beukes, 1998; Maynard, 2010; Xu et al., 2019; Freitas et al., 2021), and ultimately guiding the evolution of Earth's biosphere (Planavsky et al., 2010; Macdonald et al., 2010; Yonkee et al., 2014; Brocks et al., 2017; Hoffman et al., 2017; Nettersheim et al., 2019).

During the mid-Cryogenian Period, the South China Craton was located at ~40-60°N (Fig. 1A; Li et al., 2013). The central part of this craton was occupied by the Nanhua Basin, a semi-restricted epicratonic sea (Zhang et al., 2008; Peng et al., 2019; Cheng et al., 2021), which had limited connections to the open ocean over sills on its northeastern and (possibly) southwestern margins (Yu et al., 2016; Wang et al., 2019; Cheng et al., 2021; note: all coordinates are in the modern geographic reference frame unless otherwise noted). This intracontinental rift basin was the product of a failed rifting event during the mid-Neoproterozoic that split the South China Craton into two the Yangtze and Cathaysia blocks (Fig. 1A, B; Li et al., 2009; Song-F et al., 2020a) that later experienced compressional deformation during the Ordovician-Silurian Kwangsian Orogeny (Wang et al., 2011; Liu et al., 2016). The Neoproterozoic rifting event was associated with strong hydrothermal circulation along fault-bounded blocks within the Nanhua Basin (Pirajno, 2012; Zhou et al., 2013; Yu et al., 2016; Zhou et al., 2018; Wang et al., 2019). At the start of post-Sturtian Ice Age interglaciation (~660 Ma), the Nanhua Basin contained a reduced-salinity, high-alkalinity watermass (Yu et al., 2022) that was stratified with anoxic, saline deep waters and oxic, less saline surface waters (Lansard et al., 2012; Li et al., 2010, 2012, 2020; Zhang et al., 2015; Yu et al., 2016, 2022; Wang et al., 2019; Cheng et al., 2021).

The Cryogenian succession of the Nanhua Basin consists of (in ascending order) the Tiesi'ao, Datangpo, and Nantuo formations (Fig. 1C). The Tiesi'ao Formation comprises diamictite and sandstone deposited during the Sturtian Ice Age (~720–660 Ma), while the Nantuo Formation contains glaciomarine diamictite, siltstone, and sandstone deposited during the Marinoan Ice Age (~650–632.3 ± 5.9 Ma) (Rooney et al., 2015). The Datangpo Formation, which is conformable with both the underlying and overlying glacial units, represents sediments that accumulated during the interglacial period. The Datangpo Formation is further subdivided into three members, with the 1st Member being the oldest (Yu et al., 2016). It consists of massive Mn-carbonates (mineralogically dominated by rhodochrosite; $MnCO_3$) interbedded with Mn-bearing shales that contain high organic carbon (1.6–2.4 wt%) and abundant pyrite (FeS_2). This member represents an economically important Mn-ore deposit that is present throughout the grabens of the Nanhua Basin, with thicknesses of up to ~ 15 m. The 2nd Member of the Datangpo Formation is dominated by pyritic black shales, while the 3rd Member consists mainly of siltstone and is generally thicker than the other members (Fig. 1C).
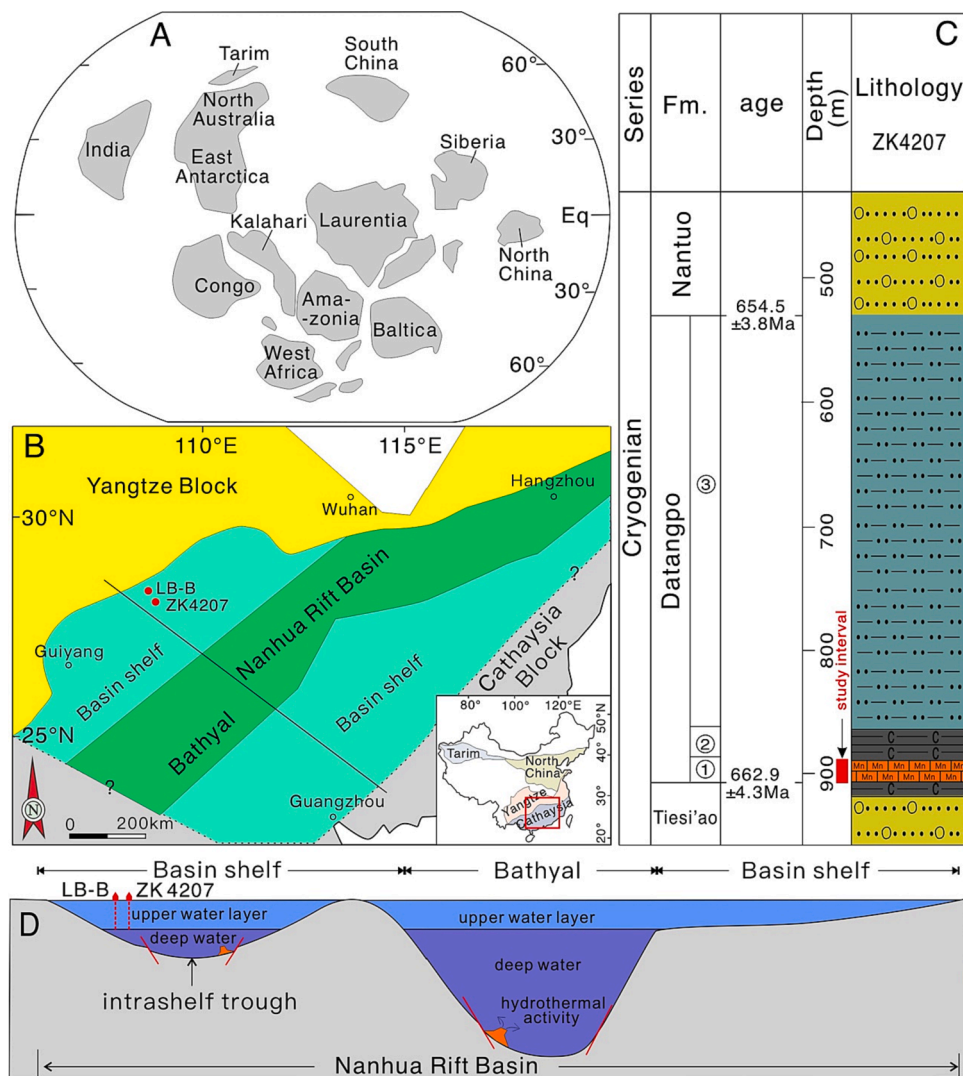
Fig. 1. (A) Global paleogeography at ~ 660 Ma (modified from Li et al., 2013); (B) Late Neoproterozoic Nanhua Rift Basin of South China, showing locations of the two study sections; (C) Stratigraphic column of drillcore ZK4207 (ages from Zhou et al., 2004, and Zhang et al., 2008); (D) Simplified cross-section of Nanhua Basin showing deep faults and zones of hydrothermal activity.

Two sites were investigated in this study: a (1) drillcore section (ZK4207, 28°2′24″N, 109°5′2″E, elev. 480 m.a.s.l.) and (2) mine tunnel section (LB-B, 28°4′20″N 108°46′36″E; elev. 109.48 m below sea level), both being located in the Songtao Graben, Wuling Subbasin, representing an intrashelf trough on the northwestern margin of the Nanhua Basin (Fig. 1B) (Peng et al., 2019; Yu et al., 2019). The study sites are located just southwest of Taiping Village, Songtao County, in northeastern Guizhou Province, with ~ 10 km separating the two sections (Fig. 1C). At both sites, the Datangpo Formation is present at depths of 800–1000 m below ground level. At ZK4207, the Datangpo Formation is 370 m thick and includes 13 m of Mn-rich strata (1st Member), 27 m of black shale (2nd Member), and 330 m of siltstone (3rd Member). At LB-B, the Datangpo Formation is 392 m thick and includes 5 m of Mn-rich strata (1st Member), 53 m of black shale (2nd Member), and 334 m of siltstone (3rd Member). In the study area, the 1st Member, which is the focus of the present study, consists of four horizontally laminated Mn-shale layers with three interbedded Mn-carbonate layers. In the ZK4207 core, we subdivided the 1st Member into a Lower Unit (895.5–901.5 m), a Middle Unit (891.5–895.5 m; equivalent to the "high boron interval", or HBI, of Yu et al., 2022), and an Upper Unit (887.8–891.5 m) based on characteristic chemostratigraphic patterns (see Section 4). Both the paleogeographic setting (Yu et al., 2016) and

sulfur isotope evidence (Wang et al., 2019) indicate that the study section accumulated below the photic zone (cf. Tyler, 2003), in the deep layer of the Nanhua Basin water column, at water depths estimated to have been ~ 200–500 m.

3. Methods

Covered thin sections of laminated Mn-ore samples were prepared for two samples, one from core ZK4207 (i.e., ZK4207-83; at 888.7 m) and one from core LB-B (i.e., LB-304; at 387.3 m). The thin-section of sample LB-304 was also analyzed by Raman spectroscopy at Szeged University, Hungary. For this study, new geochemical analyses were undertaken on samples from drillcore ZK4207, from which 29 samples were collected from the base to the top of the Mn-rich 1st Member at quasi-regular intervals of ~ 10 cm. All 29 samples were analyzed for major and trace elements, total carbon (TC) and total organic carbon (TOC), and sulfur (S), strontium (Sr) and neodymium (Nd) isotopes, a subset of 24 samples was analyzed for boron (B) content, and a subset of 14 samples for organic and inorganic carbon isotopes. Details of the analytical protocols for Raman spectroscopy, major and trace elements, B content, TIC and TOC, Sr and Nd isotopes, organic and inorganic carbon isotopes, and sulfide S isotopes are given in the Supplemental

Materials.

4. Results

4.1. Petrography and Raman analysis

Petrographic study of Mn-ore samples from the LB-B and ZK4207 cores revealed the frequent presence of laminae and mineralized organic material, which are readily observable at both low magnification in hand samples and at high magnification (×1000) in thin sections. Based on these observations, three types of laminated structures can be identified at different scales (from finest to coarsest): (1) mineralized organic laminae (~1 to 10 μm), (2) fine-grained quartz laminae (0.05–0.5 mm), and (3) laminae of various Mn-containing mineral phases (0.5 to 3 mm). These features likely represent some type of anaerobic microbial mat, possibly with admixed planktonic and in situ heterotrophic eukaryotic biomass.

The organic laminae are thin brown to black layers (often alternating) that exhibit variable density and individual thicknesses ranging from ~ 1 to 10 μm. The relative proportions of brown and black laminae vary stratigraphically, exhibiting a quasi-regular, millimeter-scale rhythmicity (Fig. 2A-C). Under high magnification (×1000), the meshwork in the matrix is composed of irregularly distributed, micrometer-

sized, rod- to vibrio-shaped microorganisms (arrow in Fig. 2D-E). Microtextural features like crinkly brown laminae and interwoven lacework of the organic laminae are the main constituents of the matrix.

Fine-grained (5–30 μm long) authigenic quartz crystals are present in discontinuous laminae (0.05–0.5 mm thick) within the Mn-carbonate matrix, as seen in high-magnification images (Fig. 2F-G). These quartz-rich laminae usually contain some rhodochrosite, and the quartz crystals are oriented parallel to bedding (Fig. 2F). Quartz precipitates are widespread, distributed along the original lamination of the sample but partially cross-cutting it in places, and associated closely with fine-grained carbonates, showing a cross-cutting structure suggestive of a diagenetic origin (Fig. 2G). Despite pervasive lamination, detrital interbeds are rare.

The Mn-rich intervals exhibit the coarsest scale of lamination, in which the Mn-mineral fractions vary at a scale of 0.5 to 3.0 mm. A 2.2-cm-thick interval of sample LB-304 was analyzed petrographically under high magnification to better assess the relationships amongst the different laminar features. This analysis revealed a regularly laminated structure consisting of five layers (dark brown-black-gray-black-dark brown) based on their color and petrographic character (Fig. 3A). Raman analysis demonstrated differences in mineral composition between the black, dark brown, and gray layers, which are enriched in kutnohorite [CaMn(CO$_3$)$_2$], calcian rhodochrosite (Ca-rhodochrosite),
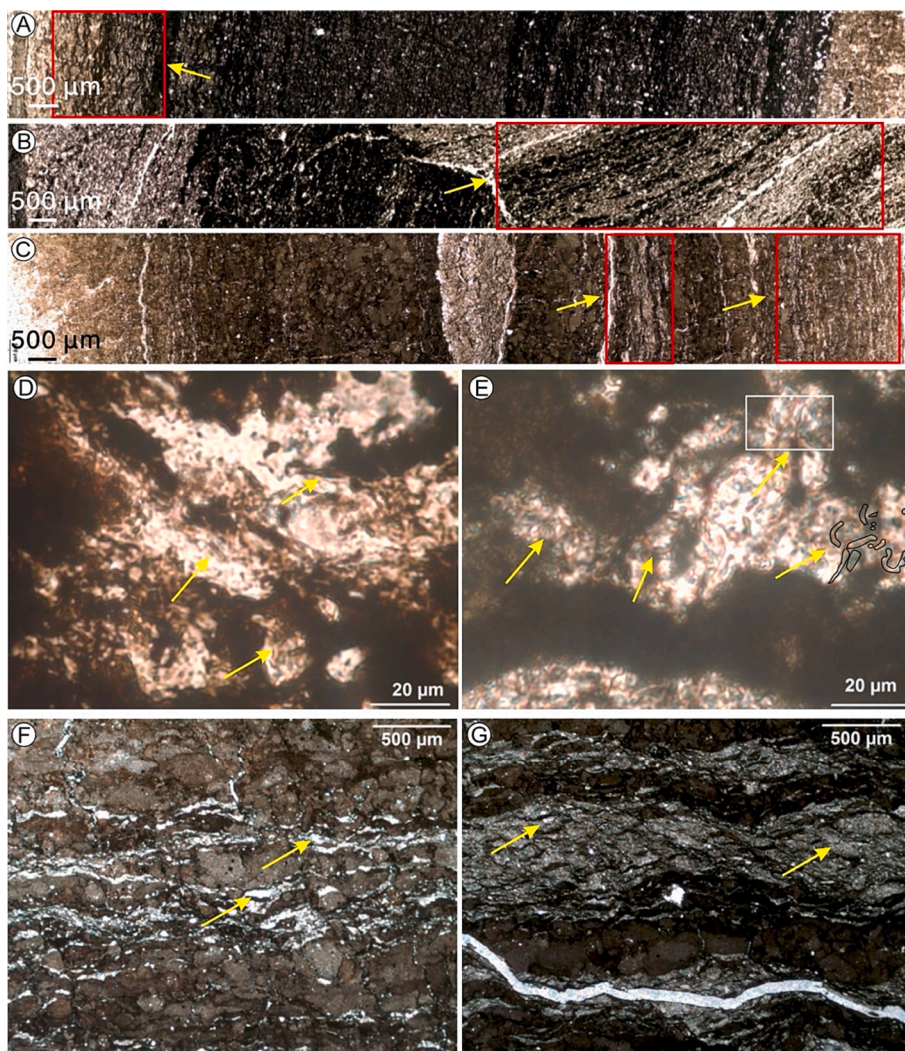

Fig. 2. Thin-section photomicrographs of Mn-carbonate samples, ZK4207-83, 888.7 m; and LB-304, 387.3 m, showing mineralized biomats and microlaminated structures (red rectangle and yellow arrow) in ZK4207 (A) and LB-B (B, C); mineralized microbially produced micro-textures (yellow arrow) in ZK4207-83 (D) and LB-304 (E); quartz precipitates (yellow arrows) and mineralized organic laminae in LB-304 (F-G).
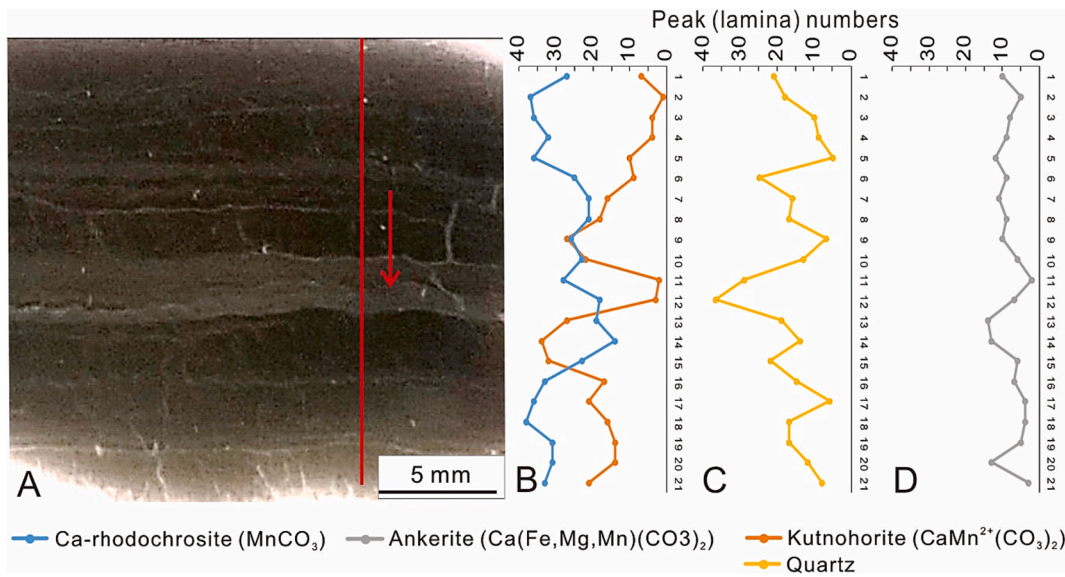
Fig. 3. (A) Thin-section of Mn-ore sample from LB-304, showing a laminated structure alternating from gray to black color; red line indicates the Raman measurement. (B-D) the number of peaks per 1 mm section for the minerals kutnohorite, Ca-rhodochrosite, quartz and ankerite.

and quartz, respectively (Fig. 3B-D). The gray and dark brown layers are characterized by extremely low kutnohorite, and the black layers by low quartz. All laminae contain relatively low ankerite, with the gray layer in the middle having the smallest amount. The black layers exhibit the highest concentrations of Mn, and the gray layer the lowest (Fig. 3B-D).

4.2. Paleosalinity proxies

Amongst the bulk-shale elemental salinity proxies proposed by Wei and Algeo (2020), Sr/Ba cannot be applied to the present study units

because of a significant positive correlation of Sr with CaO (Fig. S1; $r = +0.86$, $p(\alpha) < 0.001$), suggesting that a large fraction of Sr was sourced from the carbonate fraction. The S/TOC is not able to robustly distinguish brackish and marine salinity facies. This makes B/Ga the most promising proxy for the present study units.

The B/Ga proxy can provide information about paleosalinity conditions in fine-grained siliciclastic facies, with values of < 3, 3–6, and > 6 indicative of freshwater, brackish, and marine facies, respectively (Wei et al., 2018; Wei and Algeo, 2020). In the present study units, B/Ga ranges from 6.6 to 11.8 with a median of 8.6 (Fig. 4) (note: to avoid the
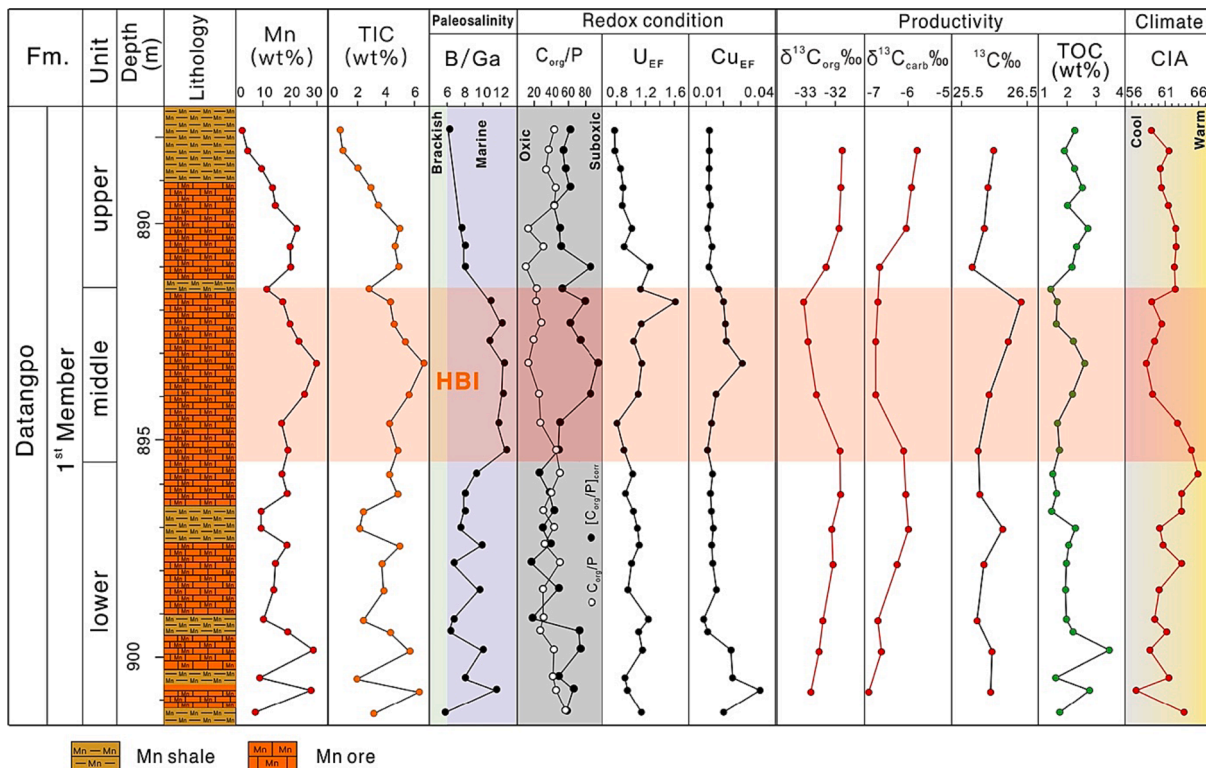

Fig. 4. Chemostratigraphic profiles of redox-, salinity-, productivity-, and climate-related proxies for the study interval in drillcore ZK4207. Note: HBI is the "high boron interval"; The white and black dots in the C_{org}/P column represent uncorrected and corrected values, respectively (see Eqs. 1 and 2).

influence of outliers, all ranges in the present study are given as 16th-84th percentiles). Median B/Ga values are higher in the Middle Unit (12.0, range 10.8–12.3) than in the Lower (median 7.9, range 6.6–9.8) and Upper units (7.7, range 6.8–7.9). These values are consistent with fully marine salinities, although possibly reflecting some degree of salinity variation around the median marine value, e.g., ~35 ± 5 psu (practical salinity unit), with somewhat higher salinities in the Middle Unit relative to the Lower and Upper units.
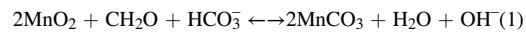
4.3. Hydrothermal proxies

Europium anomalies (i.e., Eu/Eu*$_{SN}$; Humphris and Bach, 2005) and Sr and Nd isotopes (Delacour et al., 2008) have been used as indicators of hydrothermal influence. Positive Eu anomalies with Eu/Eu*$_{SN}$ > 1.05 are often linked to reducing high-temperature hydrothermal fluids (>200 °C), in which Eu^{2+} predominates over Eu^{3+} (Bau and Dulski, 1996). In the present study, Eu/Eu*$_{SN}$ ranges from 0.83 to 1.07, with a median value of 0.93 (Fig. 5). Initial ^{87}Sr/^{86}Sr has a median (range) of 0.713003 (0.710047 to 0.75116), and initial εNd(t) has a median (range) of − 3.02 (−4.1 to − 2.4) [note: initial values calculated for 660 Ma].

Manganese contents are negatively correlated with Al$_2$O$_3$ ($r = − 0.91$; $p(\alpha) < 0.001$), reflecting a dominantly two-component mixture (i.e., Mn-carbonate and clays) of the samples (Fig. 5). Manganese shows a secular variation pattern similar to that of Eu/Eu*$_{SN}$ and ^{87}Sr/^{86}Sr$_{(660 Ma)}$, but the mirror opposite of that of εNd$_{(660 Ma)}$ (Fig. 5). Consistent with the relationships observed for Mn, Al$_2$O$_3$ variation is the inverse of that of Eu/Eu*$_{SN}$ and ^{87}Sr/^{86}Sr$_{(660 Ma)}$, but correlates positively with εNd$_{(660 Ma)}$ ($r = +0.73$; $p(\alpha) < 0.001$). ^{87}Sr/^{86}Sr$_{(660 Ma)}$ is negatively correlated with εNd$_{(660 Ma)}$ ($r = − 0.58$; $p(\alpha) < 0.001$) (Fig. 5).

4.4. Redox proxies

We evaluated redox conditions in the Datangpo Formation based on a combination of published Fe-speciation data (see Section 5.2) and elemental proxies (U$_{EF}$, Cu$_{EF}$, and C$_{org}$/P) generated in the present study (note: Mo data were unavailable). Redox-sensitive trace elements (RSTE) are generally less soluble under reducing than under oxidizing conditions, resulting in marked sedimentary enrichments in anoxic facies (Tribovillard et al., 2006). This generalized behavior makes RSTE enrichment factors (e.g., Cu$_{EF}$, U$_{EF}$, and V$_{EF}$) useful as paleoredox proxies (Algeo and Maynard, 2008), with a robustness that substantially exceeds that of bimetal ratio proxies (e.g., Ni/Co, V/Ni; Algeo and Liu, 2020). Amongst the redox-sensitive trace elements (RSTEs), we focused on U$_{EF}$ and Cu$_{EF}$, which yielded median values (ranges) of 1.02 (0.89–1.15) and 1.06 (0.91–1.69), respectively (Figs. 4, 6B). These values suggest no significant authigenic enrichment, consistent with oxic or anoxic-ferruginous conditions prevailing in the depositional system.

C$_{org}$/P is another widely used paleoredox proxy that is based on redox-dependent differences in retention patterns of organic C and P in the sediment during remineralization of organic matter (Algeo and Ingall, 2007; Kraal et al., 2010; Song-J et al., 2020b). In the present study units, raw (uncorrected) C$_{org}$/P ratios range from 22 to 45 with a median of 32 (Figs. 4, 6A). Since reduction of Mn(IV) to Mn(II) followed by precipitation of Mn-carbonate is generally associated with the decomposition of organic matter in the study interval (Yu et al., 2016), we calculated corrected C$_{org}$/P ratios (i.e., [C$_{org}$/P]$_{corr}$) to account for organic carbon loss:

$$2MnO_2 + CH_2O + HCO_3^- \leftrightarrow 2MnCO_3 + H_2O + OH^- (1)$$

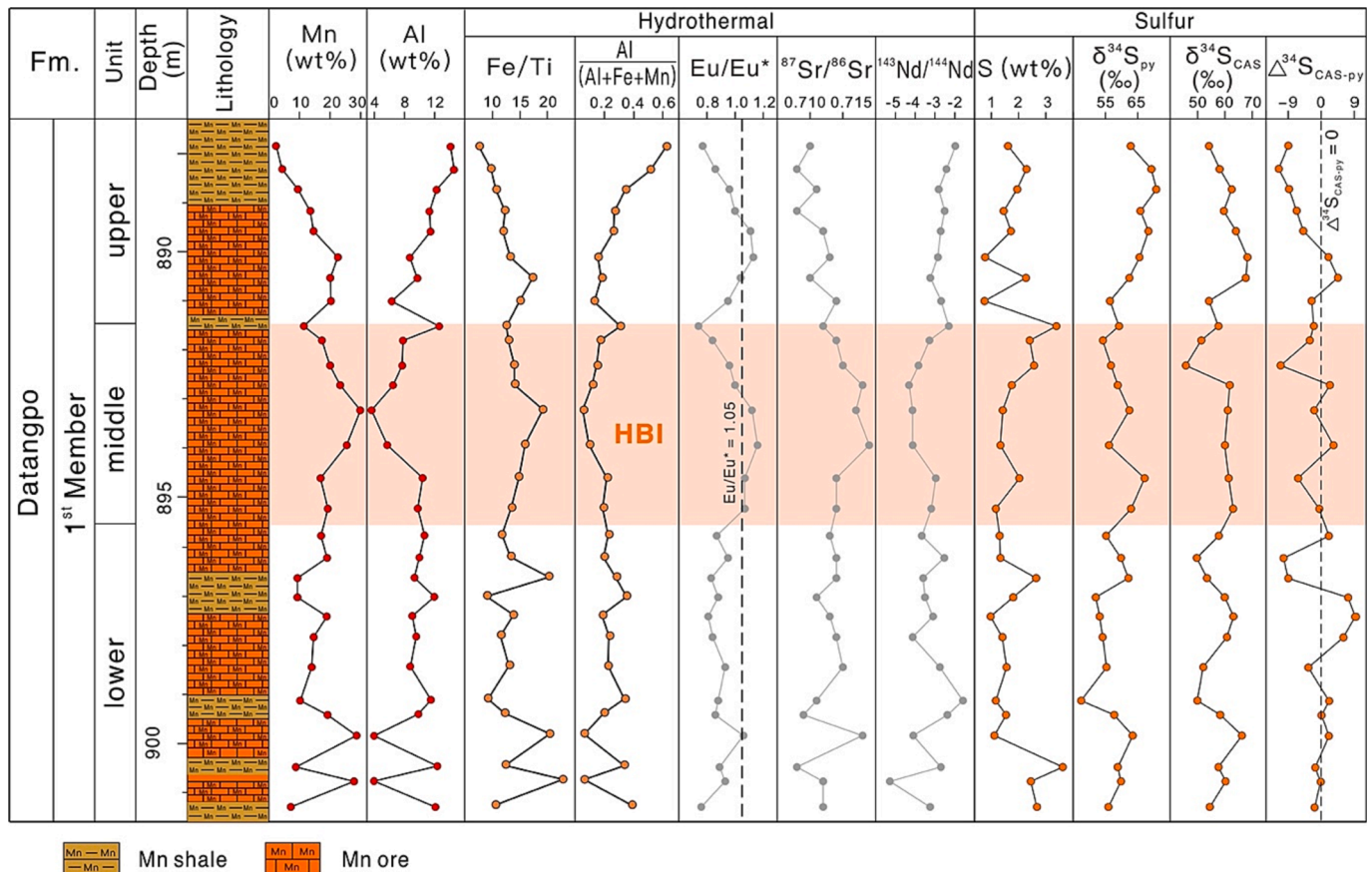$$[C_{org}/P]_{corr} = (C_{org} + Mn/2) / P (2)$$

Fig. 5. Chemostratigraphic profiles of Mn, Al, hydrothermal-, and sulfur-related proxies for the study interval in drillcore ZK4207.
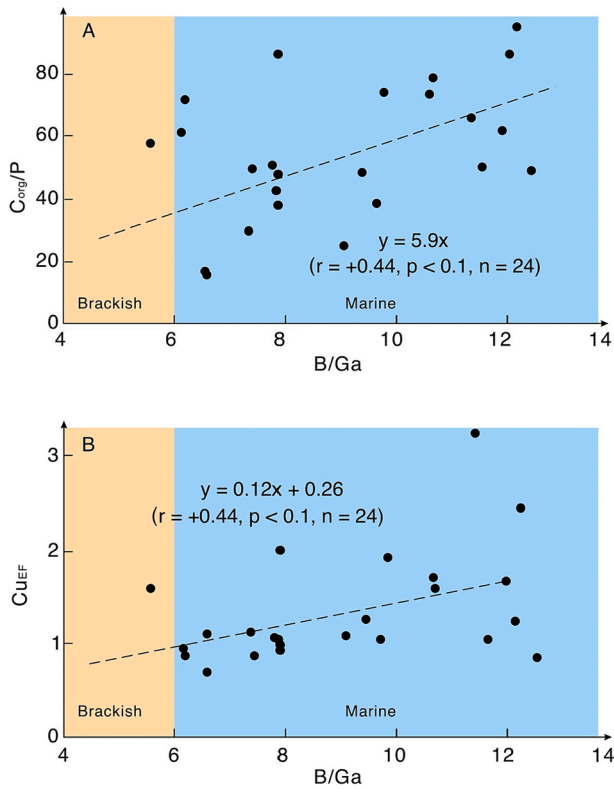
Fig. 6. B/Ga versus (A) C_{org}/P and (I) Cu_{EF} for drillcore ZK4207.

where all species are in moles, and one-half mole of organic carbon is oxidized for each mole of $MnCO_3$ that is formed. In the study units, $[C_{org}/P]_{corr}$ ranges from 38 to 73 with a median value of 52. All three proxies (i.e., $[C_{org}/P]_{corr}$, Cu_{EF}, and U_{EF}) exhibit distinctly higher values in the Middle Unit [i.e., medians (ranges) of 67 (50–85), 1.5 (1.1–1.7), and 1.1 (0.92–1.1), respectively] than in the Lower [i.e., 42 (24–66), 1.1 (1.0–1.9), and 1.0 (0.9–1.1)] and Upper units [i.e., 55 (49–61), 0.93 (0.91–0.98), and 0.89 (0.79–1.0)] (Fig. 4).

The profiles of the three independent redox proxies utilized in this study (i.e., $[C_{org}/P]_{corr}$, Cu_{EF}, and U_{EF}) display similar stratigraphic patterns (Fig. 4). Manganese content shows significant positive correlations with $[C_{org}/P]_{corr}$ ($r = +0.48$; $p(\alpha) < 0.01$) and Cu_{EF} ($r = +0.48$; $p(\alpha) < 0.01$) but only a weak and statistically non-significant positive correlation with U_{EF} ($r = +0.29$; $p(\alpha) = 0.13$).

4.5. TOC, TIC and carbon isotopes

TOC ranges from 1.6 to 2.4 wt% with a median of 2.0 wt%, while TIC ranges from 2.3 to 5.1 wt% with a median of 4.2 wt%. The $\delta^{13}C_{org}$ and $\delta^{13}C_{carb}$ have medians (ranges) of -32.22 ‰ (-32.82 to -31.82 ‰) and -6.43 ‰ (-6.72 to -6.00 ‰) respectively, yielding a relatively constant $\Delta^{13}C$ of 25.90 ‰ (25.75 to 26.12 ‰). $\delta^{13}C_{org}$ and $\delta^{13}C_{carb}$ exhibit distinctly lower values in the Middle Unit [i.e., medians (ranges) of –32.8 ‰ (–33.0 to –32.2 ‰) and –6.71 ‰ (–6.74 to –6.67 ‰), respectively] than in the Lower [i.e., –32.3 ‰ (–32.6 to –32.2 ‰) and –6.4 ‰ (–6.7 to –6.0 ‰)] and Upper units [i.e., –31.84 ‰ (–32.10 to –31.78 ‰) and –6.0 ‰ (–6.4 to –5.9 ‰)] (Fig. 4).

TIC shows nearly the same pattern as manganese content (Fig. 4), with strong positive covariation ($r = +0.97$; $p(\alpha) < 0.01$). Manganese contents are positively correlated with TOC ($r = +0.50$; $p(\alpha) < 0.01$), and show a moderate, negative correlation with $\delta^{13}C_{carb}$ ($r = -0.61$; $p(\alpha) < 0.05$) and $\delta^{13}C_{org}$ ($r = -0.50$; $p(\alpha) = 0.07$) (). $\delta^{18}O$ ranges from -10.17 to -9.07 ‰, with a median of -9.59 ‰, and exhibits a non-significant correlation with Mn content ($r = +0.28$; $p(\alpha) = 0.33$). TOC exhibits a non-significant correlation with $\delta^{13}C_{org}$ ($r = -0.20$; $p(\alpha) =$

0.49).

5. Discussion

The metallogenesis of Mn-carbonates of the Cryogenian Datangpo Formation has been extensively investigated, including the roles of redox fluctuations (Yu et al., 2016), hydrothermal activity (Zhou et al., 2013), microbial processes (Yu et al., 2019), hydrography (Dellwig et al., 2012; Varentsov, 2013; Cheng et al., 2021), and alkalinity sources (Yu et al., 2022). However, the focus of some of these studies was on a single aspect of the Datangpo manganese deposits, which has hindered a comprehensive understanding of the mechanisms of Mn-carbonate formation in the Datangpo Formations and other carbonate-hosted Mn deposits. Here, we evaluate how salinity, redox, and productivity variations in the postglacial Nanhua Basin (Sections 5.1-5.3) might have collectively contributed to Mn enrichment, and we glean new insights into the sources of Mn and the possible role of microbial activities (Sections 5.4-5.6). Finally, we integrate our observations and interpretations to generate a revised model of Mn-carbonate formation in the postglacial Nanhua Basin (Section 5.7).

5.1. Salinity conditions

The Cryogenian Nanhua Basin has long been regarded as a fully marine basin (e.g., Wang and Li, 2003; Zhang et al., 2015), although a degree of watermass restriction in deep graben areas has been inferred from geochemical and petrographic data (Li et al., 2012; Yu et al., 2016). Post-Sturtian shallow-water cap carbonates record $\delta^{13}C$ trends similar to those in coeval sections globally (Halverson et al., 2002; Macdonald et al., 2010; Johnston et al., 2012), arguing for a robust connection to the global ocean (Wang et al., 2019). The weight of existing evidence thus favors no more than semi-restriction of the Nanhua Basin watermass.

The water column of the post-Sturtian Nanhua Basin was salinity- and redox-stratified, with an oxic, reduced-salinity surface layer and a reducing, normal-marine-salinity deep layer (Lansard et al., 2012; Li et al., 2012; Cheng et al., 2021; Yu et al., 2022). Such stratification patterns normally depend on the overall hydrological balance of a basin (i.e., precipitation and runoff versus evaporation), and the rate at which watermass is exchanged with the open ocean (Anadón et al., 2002; Algeo et al., 2008; Savenije, 2012; Wei et al., 2020). Owing to the influx of alkaline glacial meltwater, the surface layer may have had higher alkalinity than the deep layer (Yu et al., 2022).

Among elemental salinity proxies for fine-grained siliciclastic sediments, the B/Ga proxy yields the most consistent and robust interpretations (Wei and Algeo, 2020). Although low siliciclastic content may yield excessively high B/Ga ratios (Cheng et al., 2023), the 1st Member of the Datangpo Formation exhibits a relatively uniform lithologic composition, consisting mainly of Mn-carbonate with minor intercalations of thin Mn-shale layers. A moderate positive B-Al correlation ($r = +0.43$; $p(\alpha) < 0.1$) indicates that boron is associated with the clay fraction. Gallium is also associated with the clay fraction, as shown by a strong Ga-Al correlation ($r = +0.93$; $p(\alpha) < 0.001$). Thus, B was normalized to Ga, and the B/Ga ratio can be utilized as a proxy for watermass salinity (Wei and Algeo, 2020). Ga content is nearly constant through the whole study section (median 13.2 ppm, range 9.2–18 ppm), whereas B varies significantly, averaging ~ 100 ppm but rising to ~ 170 ppm within the HBI. Thus, the lithology of the study section does not significantly influence the paleosalinity signals documented by the B/Ga proxy.

The B/Ga values of the ZK4207 core (Fig. 4) indicate generally marine salinities, although with some degree of variation around the typical mean value, e.g., $\sim 35 \pm 5$ psu. The B/Ga profile of the study core exhibits a considerable degree of stratigraphic coherence, with somewhat higher salinities in the Middle Unit (i.e., the HBI) relative to the Lower and Upper units. The B/Ga values of the Lower and Upper units

are typical of normal-marine environments (Wei and Algeo, 2020; Wei et al., 2022) although a reduction in salinity related to glacial meltwater influx might have occurred transiently during the Sturtian deglaciation (cf. Dierssen et al., 2002; Anadón et al., 2002), as possibly indicated by B/Ga values as low as 5.63 in the Lower Unit and the generally upward decreasing B/Ga trend within the Upper Unit.

The comparatively elevated B/Ga values of the Middle Unit (i.e., the "high boron interval", or HBI, of Yu et al., 2022) suggest either salinities somewhat above normal marine (i.e., hypersaline) or an additional B source to the Nanhua Basin (Fig. 4). One possibility is development of a hypersaline watermass, as evaporation concentrates aqueous B with little change in Ga (which primarily resides in the detrital fraction) (Wei and Algeo, 2020). However, strong evaporation in the mid-Cryogenian Nanhua Basin is unlikely given its probable location at temperate paleolatitudes (Fig. 1A) and the absence of sedimentological or mineralogical evidence for hypersaline conditions. Alternatively, excess B may have been supplied by hydrothermal sources, as indicated by significant correlations of B/Ga with the hydrothermal proxies Eu/Eu* ($r = +0.61$; $p(\alpha) < 0.01$), $^{87}Sr/^{86}Sr_{(660\ Ma)}$ ($r = +0.63$; $p(\alpha) < 0.01$), and $\varepsilon Nd_{(660\ Ma)}$ ($r = -0.56$; $p(\alpha) < 0.01$). We infer that the most likely cause of elevated B/Ga ratios in the Middle Unit was inputs of hydrothermally sourced B (Yu et al., 2022), and such inputs may have been accompanied by a rise in the salinity of the Nanhua Basin watermass (cf. Noll et al., 1996; Pirajno, 2012; Zhou et al., 2013, 2018).

5.2. Redox conditions

Redox conditions during deposition of the Datangpo Mn-ore deposits have received extensive study. While early metallogenic models inferred a link between Mn-carbonate precipitation and episodic oxygenation events (Yu et al., 2016; Xiao et al., 2017, 2019), more recent Fe-speciation studies have inferred uniformly anoxic conditions (Ye et al., 2018; Ma et al., 2019; Cheng et al., 2020; Tan et al., 2021). A detailed Fe-speciation record for the study units was generated by compiling data from the Lijiawan (Li-T et al., 2022), the Xixibao, Gaodi, and Changxingpo (Cheng et al., 2021), and the Daotuo sections (Wei et al., 2020). These sections are all located in the same graben (or subbasin) as the ZK4207 core, their distances from that core being no more than 15 km (and only 3 km for Xixibao). Because of their mutual proximity, the Fe-speciation results obtained in these earlier published studies are applicable to the present study units and allow for the development of a local understanding of redox conditions. The Fe_{py}/Fe_{HR} of the Mn-carbonate interval from the Gaodi, Xixiao, Changxingpo and Daotuo sections have median (range) values of 0.56 (0.09–0.77), 0.58 (0.43–0.67), 0.61 (0.58–0.80), and 0.61 (0.22–0.71) respectively (Wei et al., 2020; Cheng et al., 2021) (Fig. 7). Li-T et al. (2022) also reported Fe_{py}/Fe_{HR} value of
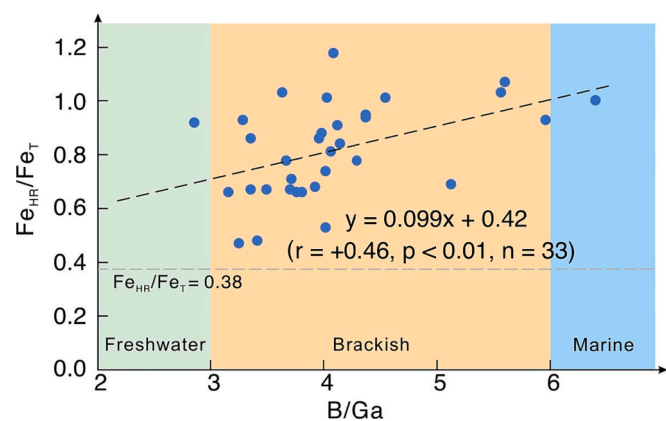

Fig. 7. Fe_{HR}/Fe_T versus B/Ga for the Gaodi section (data from Cheng et al., 2021). Note: the interval at Gaodi for which data is plotted is equivalent to the study interval in drillcore ZK4207.

0.5 for a Mn-carbonate sample from Lijiawan Section. Fe-speciation data of Mn-carbonate samples from these five different sections suggest a uniform and dominantly ferruginous-anoxic condition during deposition (Li-T et al., 2022; Wei et al., 2020; Cheng et al., 2021), with black shale intervals characterized by euxinic-anoxic conditions (Cheng et al., 2021).

Redox proxies in the present study, i.e., $[C_{org}/P]_{corr}$ (Fig. 4), Cu_{EF} and U_{EF} (Fig. 5), indicate non-euxinic conditions (See Section 4.4). In addition to the present study, similar C_{org}/P, Cu_{EF} and U_{EF} have been recorded within equivalent Mn-carbonate intervals of sections elsewhere: C_{org}/P in ZK0408 from Xiushan has a median (range) value of 46.2 (15.1–111) (Ai et al., 2021); the Changxingpo and Xixibao sections record U_{EF} of 1.39 (1.25–1.44) and 1.69 (1.06–2.25) respectively (Pan et al., 2021); a section from Songtao County produced Cu_{EF} and U_{EF} of 2.56 (1.67–4.09) and 1.62 (1.33–2.12) respectively (Tan et al., 2021). Given low atmospheric and ocean oxygen levels during the Cryogenian (Wallace et al., 2017), the strong stratification of the Nanhua Basin is likely to have predisposed its deep waters toward anoxia (Lansard et al., 2012; Li et al., 2012). The redox proxy data of the present and earlier studies most parsimoniously indicate a uniformly ferruginous-anoxic deep-water redox condition during deposition of the Mn-carbonate interval of the Datangpo Formation.

5.3. Primary productivity conditions

Primary productivity is another fundamental parameter of aquatic ecosystems, playing a pivotal role in ecological energetics, nutrient-element cycling, and environmental redox conditions (Falkowski et al., 1998; Schoepfer et al., 2015; Middelburg, 2019). Primary production is thought to have been high in the Nanhua Basin during the post-Sturtian interval owing to rising sea levels and a greater nutrient supply from a connection with the open ocean (Li et al., 2012; Ai et al., 2021; cf. Lyons et al., 2003). High productivity is supported by the high TOC content and evidence of intense benthic microbial activity observed in the thin section of samples from Mn-ore intervals of Datangpo Formation (Fig. 2) (Ye et al., 2018; Yu et al., 2016; Ma et al., 2019). To this end, decomposition of abundant organic matter may have contributed to the production of alkalinity (HCO_3^- and CO_3^{2-}) essential for Mn-carbonate precipitation (Neumeister et al., 2016, 2020; Wittkop et al., 2022).

Primary productivity in paleodepositional systems can be evaluated quantitatively based on organic carbon accumulation rates (OCAR) (Algeo et al., 2013; Schoepfer et al., 2015). OCAR is calculated as TOC $\times$ $\rho \times$ LSR, where ρ is sediment density and LSR is linear sedimentation rate. Based on radiometric ages and strata thicknesses, LSRs in the Datangpo Formation range from 8.8 to 88 m Myr^{-1} with a mean of 48 m Myr^{-1}, or $\sim$ 0.05 mm yr^{-1} (Yu et al., 2016). Given typical densities for Mn-carbonate (3.12 g/cm^3) and shale (2.06–2.67 g/cm^3), we adopted an average density of 2.7 g/cm^3 for the Mn-ore samples, which consist of mixtures of carbonate and clays. On this basis, we calculated an average OCAR of 47 $\times$ 10^3 mg $C/cm^2/kyr$, which is higher than the primary production estimated for $\sim$ 90 % of modern shelf settings documented in Longhurst et al. (1995; see table 2 in Schoepfer et al., 2015).

Carbon isotopes provide further insights into productivity and carbon cycling. The parallel changes in $\delta^{13}C_{carb}$ and $\delta^{13}C_{org}$ through drillcore ZK4207 (Fig. 4) suggest that: (1) primary signals are preserved with little or no diagenetic overprint (Meyer et al., 2013); (2) the offset between $\delta^{13}C_{carb}$ and $\delta^{13}C_{org}$ (i.e., $\Delta^{13}C_{carb-org}$) reflects photosynthetic fractionation (Hayes et al., 1999; Johnston et al., 2012); and (3) terrestrial plant inputs played no role during the Neoproterozoic (Burdige, 2007; Peng et al., 2019), although land-based microbial mats were likely important (Lalonde and Konhauser, 2015; Planavsky et al., 2021). These observations support interpretations of the $\delta^{13}C_{carb}$ and $\delta^{13}C_{org}$ records in terms of changes in marine primary productivity rates, although probably at a global scale and not just within the Nanhua Basin itself.

Regional primary productivity rates in the Nanhua Basin were also

likely influenced indirectly by hydrothermal activity, as suggested by a significant positive correlation between TOC and Eu/Eu* ($r = +0.45$, p (α) < 0.01) (Supplemental data). Hydrothermal activity can deliver excess nutrients to a basin for both deep-water chemosynthesis and surface-layer photosynthesis (e.g., McCollom, 2000; Boyd and Ellwood, 2010; Resing et al., 2015; Jenkyns, 2010; Gomez-Saez et al., 2017; Stüeken et al., 2023). Alternatively (or additionally), enhanced deglacial/postglacial weathering of continental regolith may have supplied excess nutrients and fueled primary production during deposition of the study interval (cf. Planavsky et al., 2010; Swanson-Hysell et al., 2010). The negative shift (ca. –1 ‰) of carbon isotopes during the HBI probably indicates introduction of ^{13}C-depleted carbon into the basin by hydrothermal activity, possibly in the form of thermogenic methane and/or CO_2 (Frieling et al., 2016).

Watermass salinity was related, either directly or indirectly, to primary productivity in the Nanhua Basin, as shown by negative correlations of B/Ga with $\delta^{13}C_{carb}$ ($r = -0.45$, $n = 12$; $p(\alpha) = 0.14$) and $\delta^{13}C_{org}$ ($r = -0.40$, $n = 12$; $p(\alpha) = 0.20$) (Fig. 8). Possibly, the correlation of B/Ga with $\delta^{13}C_{carb}$ is incidental, deriving from independent relationships of Mn to $\delta^{13}C_{carb}$ and B/Ga. Yet two mechanisms may link watermass salinity with primary productivity: (1) salinity variation may affect the mass, composition, and distribution of the phytoplankton community within an ecosystem (Little et al., 2017); and (2) water-column stratification due to vertical salinity variations enhances deep-water anoxia and, thus, organic matter preservation, and it may also influence surface-water productivity through suppression of nutrient upwelling (Almogi-Labin et al., 1993).

5.4. Relationship of Mn precipitation to water-column stratification in the Nanhua Basin

The transfer of Mn^{2+} to the sediment depends critically on watermass redox conditions. Mn is normally in dissolved form under anoxic to euxinic to ferruginous-anoxic conditions, but it is readily removed from the water column to the sediment by precipitation of solid-phase Mn (IV)-oxides or hydroxides under oxic conditions (Bender et al., 1977;

Wedepohl, 1978; Frakes and Bolton, 1992; Rio-Salas et al., 2013; Kuleshov, 2017; Li-WJ et al., 2022). In a stratified water column, two standard models exist for Mn-carbonate formation: (1) the "diagenetic model", in which aqueous manganese is precipitated as solid-phase Mn (IV)-oxyhydroxides in the upper oxic layer, sinks to the seafloor and becomes reductively dissolved, and is then reprecipitated as Mn(II)-carbonate minerals—a process that is commonly mediated by heterotrophic microbial activity that involves oxidation of organic matter during the early diagenetic stage (Okita et al., 1988; Fan et al., 1992; Polgári et al., 2012a, 2012b, 2016, 2019; Neumeister et al., 2016, 2020; Yu et al., 2016, 2019; Li et al., 2022; Yan et al., 2022; Dong et al., 2023); and (2) the "direct precipitation model", in which Mn^{2+} in anoxic deep waters reacts directly with HCO_3^-, precipitating Mn-carbonate minerals whose solubility product (K_{sp}) is exceeded (Pingitore et al., 1988; Herndon et al., 2018; Wittkop et al., 2020).

Mn precipitation in the Nanhua Basin was strongly influenced by the prevailing salinity-redox-productivity conditions and their relationship to water-column stratification. The development of stratification, linked to vertical variation in water-column salinity, was a dominant control on: (1) the redox status of the deep watermass (Cheng et al., 2021), and (2) the upwelling of nutrients and, thus, primary productivity rates and the sinking flux of organic matter on which the microbial community that catalyzed Mn-carbonate precipitation depended (Yu et al., 2019). The close relationships between Mn content and the redox proxies C_{org}/P ($r = +0.48$, $p(\alpha) < 0.1$), Cu_{EF} ($r = +0.44$, $p(\alpha) < 0.1$) and Fe_{HR}/Fe_T ($r = +0.46$, $p(\alpha) < 0.01$) indicate that Mn-ore deposition was strongly modulated by redox conditions, being favored by more reducing conditions. Positive covariation of these redox proxies with the B/Ga salinity proxy ($r = +0.44$, $+0.44$ and $+0.46$, respectively; $p(\alpha) < 0.1$) (Figs. 6, 7) further supports a close relationship between watermass salinity and deep-water redox conditions, and their links to Mn-ore deposition, even though there is no significant correlation between B/Ga and Fe_{py}/Fe_{HR}.

Fluctuations of watermass salinity and redox conditions within the Nanhua Basin led to alternations between high-salinity ferruginous conditions that favored Mn-carbonate precipitation and low-salinity euxinic conditions that favored Mn-rich black shale accumulation (Fig. 5; cf. Cheng et al., 2021). Increases in watermass salinity and primary production were linked to Mn-carbonate formation in several ways. First, salinity rises linked to either seawater influx or hydrothermal emissions are likely to have provided nutrients, leading to an increased OM flux initiated by enhanced primary production, and which, in turn, fueled the microbial metabolisms that catalyze precipitation of Mn-carbonates (Okita, 1992; Polgári et al., 2012a, 2012b, 2016, 2019; Yu et al., 2019). Second, intensified water-column stratification linked to a salinity gradient would have enhanced bottom water anoxia and, thus, organic matter preservation. These relationships are reflected in significant correlations of Mn with TOC ($r = +0.50$, $p(\alpha) < 0.01$), $\delta^{13}C_{org}$ ($r = -0.50$, $p(\alpha) < 0.1$) and $\delta^{13}C_{carb}$ ($r = -0.61$, $p(\alpha) < 0.05$; Fig. S2), suggesting that primary production and organic carbon sinking fluxes were related to the rate of Mn-carbonate precipitation. Third, anaerobic decomposition of organic matter generates abundant alkalinity in the form of CO_3^{2-} and HCO_3^- for precipitation of Mn-carbonate minerals such as rhodochrosite (Neumeister et al., 2015, 2016, 2020). The low $\delta^{13}C_{carb}$ values of the Mn-rich Middle Unit imply massive organic matter decomposition, which would have promoted precipitation of Mn-carbonates by providing large amounts of extra alkalinity (e.g., CO_3^{2-} and HCO_3^-). Thus, a combination of enhanced primary production, organic matter influx, high alkalinity and reducing (i.e., ferruginous) conditions created a favorable environment for formation of Mn-carbonate deposits through either the "diagenetic model" or the "direct precipitation model", although the former mechanism is likely to have been dominant in the Cryogenian Nanhua Basin (see Section 5.6).
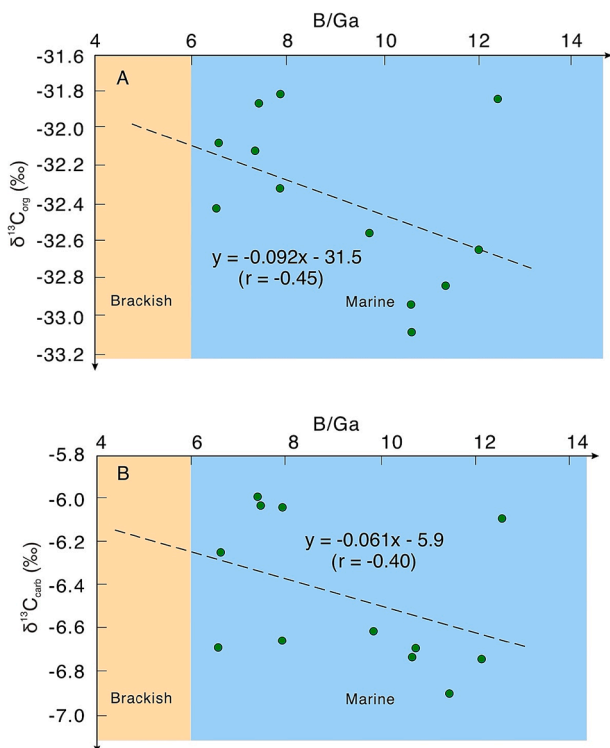

Fig. 8. B/Ga versus (A) $\delta^{13}C_{org}$ and (B) $\delta^{13}C_{carb}$ for drillcore ZK4207.

5.5. Mn sources and hydrothermal activities

Various sources of manganese have been proposed for formation of Mn-carbonate deposits, including riverine inputs (mainly particulate Mn) (Bender et al., 1977; Slemons et al., 2010), hydrothermal vents (mainly dissolved Mn) (Usui et al., 1986; Mandernack and Tebo, 1993; Camprubí et al., 2008; Hulten et al., 2017), and aeolian dust (particulate Mn) (Guieu et al., 1994; Mendez et al., 2010) (Fig. 9). For the Cenozoic Ocean, Glasby (1988) estimated that 90 % of the Mn inventory was sourced from hydrothermal venting. For this reason, deep waters generally have higher concentrations of Mn^{2+}, a condition that can be enhanced under reducing conditions owing to the high solubility of Mn (II). Consequently, the abyssal seafloor serves as a locus for Mn accumulation (Bazilevskaya, 2006), e.g., in the form of manganese crusts near oceanic spreading centers (Narejo et al., 2019). Evidence for hydrothermal exhalative events in the Cryogenian Nanhua Basin has been extensively documented (e.g., Zhang et al., 2015; Wu et al., 2016; Zhou et al., 2018; Wang et al., 2019). Hydrothermal activity would have led to a watermass that was strongly enriched in Mn^{2+} given the low atmospheric oxygen levels of the Cryogenian and the limitation of atmospheric-oceanic gas exchange caused by Snowball-Earth ice shelves (Li et al., 2012; Zhang et al., 2015; Yu et al., 2016). It is worth noting that low atmospheric pO_2 during the Cryogenian could have also permitted large erosional fluxes of Mn^{2+} from continents to oceans through weathering, a process enhanced by glaciation (e.g., Mn deposits of the Santa Cruz Formation; Freitas et al., 2021).

Covariation between Nd and Sr isotopes is commonly effective at fingerprinting the sources of geomaterials. In our dataset, εNd and $^{87}Sr/^{86}Sr$ show significant negative and positive correlations with Mn, and significant positive and negative correlations with Al_2O_3, respectively. These observations demonstrate that Nd and Sr in the study units have two sources with distinctly different isotopic compositions, one source being dominant in the Mn-carbonates and the other in the clay fraction. The source dominating the Mn-carbonates was a non-detrital component characterized by low εNd and high $^{87}Sr/^{86}Sr$, consistent with hydrothermal inputs from old upper crustal systems (DePaolo and Wasserburg, 1979) but not from deep crustal and mantle reservoirs (White, 2023). Conversely, the source dominating the Mn-rich shales was a detrital component characterized by high εNd and low $^{87}Sr/^{86}Sr$, suggesting erosion of relatively young (juvenile) crustal materials (Yu et al., 2016, 2019).

In the ZK4207 study section, Mn covaries positively with $Eu/Eu*_{SN}$ ($r = +0.64$, $p(\alpha) < 0.01$) and $^{87}Sr/^{86}Sr_{(660\ Ma)}$ ($r = +0.69$, $p(\alpha) < 0.01$) and inversely with $\varepsilon Nd_{(660\ Ma)}$ ($r = -0.63$, $p(\alpha) < 0.01$) (Figs. 10, S2). The covariant relationships of Mn to these hydrothermal proxies (see Section 4.2) suggest that Mn(II) accumulating in the sediment as deep-water Mn-carbonates was primarily hydrothermally sourced (cf. Peter and Goodfellow, 1996). On an Fe/Ti versus Al/(Al + Fe + Mn) discriminant plot, ~90 % of study samples fall within the hydrothermal field (Fig. 10C; Marchig et al., 1982; Boström, 1983), providing further support for strong hydrothermal influences. This relationship is underscored by significant correlations of Fe/Ti and Al/(Al + Fe + Mn) with the other hydrothermal proxies: $Eu/Eu*_{SN}$ ($r = +0.40$, $p(\alpha) < 0.05$; $r = -0.58$, $p(\alpha) < 0.01$), $^{87}Sr/^{86}Sr_{(660\ Ma)}$ ($r = +0.50$, $p(\alpha) < 0.01$; $r = -0.68$, $p(\alpha) < 0.01$), and $\varepsilon Nd_{(660\ Ma)}$ ($r = -0.67$, $p(\alpha) < 0.01$; $r = +0.63$, $p(\alpha) < 0.01$, respectively). High total sulfur contents (mean 1.9 ± 0.7 %) and frequent negative $\triangle^{34}S$ values provide additional support for hydrothermal activity in the Nanhua Basin (Fig. 4; Wang et al., 2019). Although hydrothermal fluxes were almost certainly the dominant source of Mn to the Nanhua Basin, other sources (e.g., terrestrial weathering) may have contributed a minor fraction (Fig. 10C). Finally, the similar elemental chemistry of these Mn-bearing rocks to those of modern hydrothermal sediments (Fig. 6 in He et al., 2014), as well as their relatively high depositional temperatures (~200 °C), as reconstructed from quartz-inclusion and bitumen reflectance data from the manganese ores, support a link to hydrothermal activity (Chen and
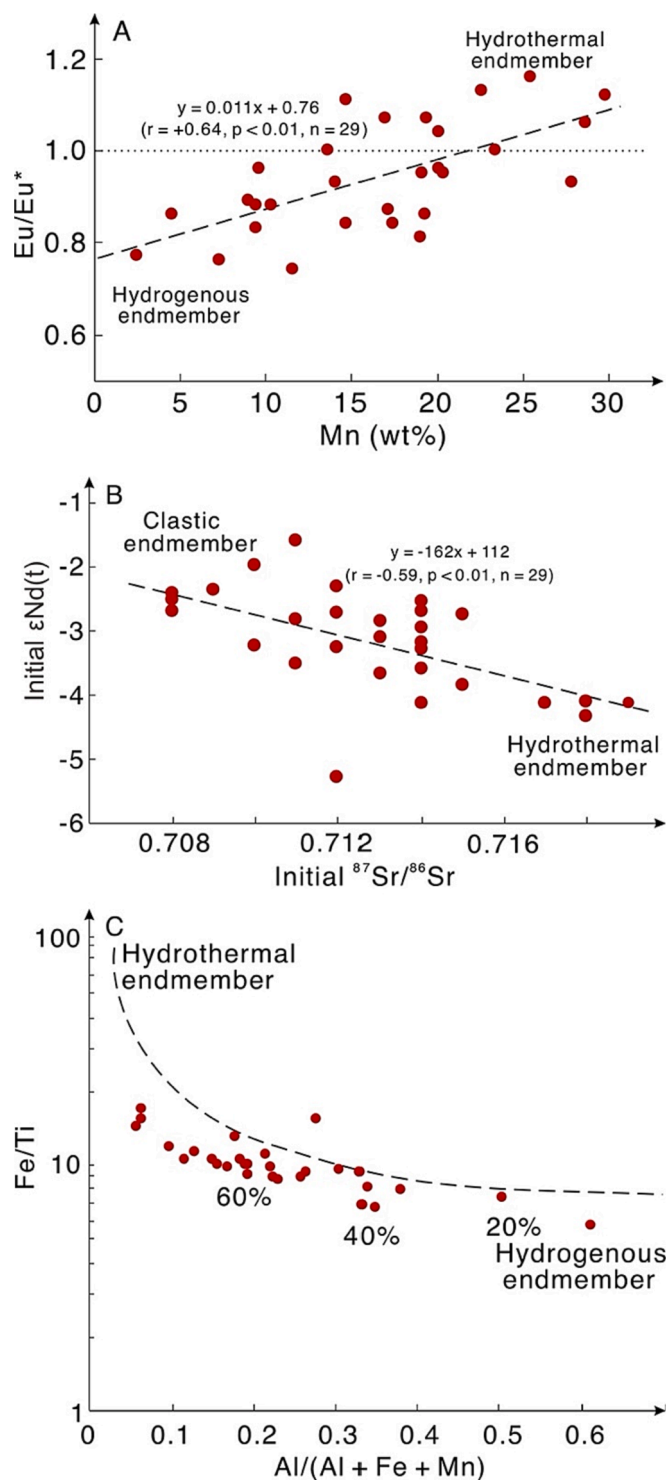
Fig. 9. Discriminant plots of proxies with mixed hydrothermal and hydrogenous (or clastic) origins for the study interval in drillcore ZK4207. (A) $Eu/Eu*_{SN}$ versus Mn (Peter and Goodfellow, 1996). (B) $^{87}Sr/^{86}Sr_{(660\ Ma)}$ versus $\varepsilon Nd_{(660\ Ma)}$. (C) Fe/Ti versus Al/(Al + Fe + Mn). Values on the two-component mixing line represent the percentage of hydrothermal contribution (Marchig et al., 1982; Boström, 1983).

Chen, 1992; He et al., 2014).

In the Nanhua Basin, the spatial distribution of Mn-ore deposits is closely associated with the fault zones that delineate the NE-SW-trending horsts and grabens defining the deep structure of the basin (Wang and Li, 2003; Zhou et al., 2013, 2018; Wang et al., 2019; table 1
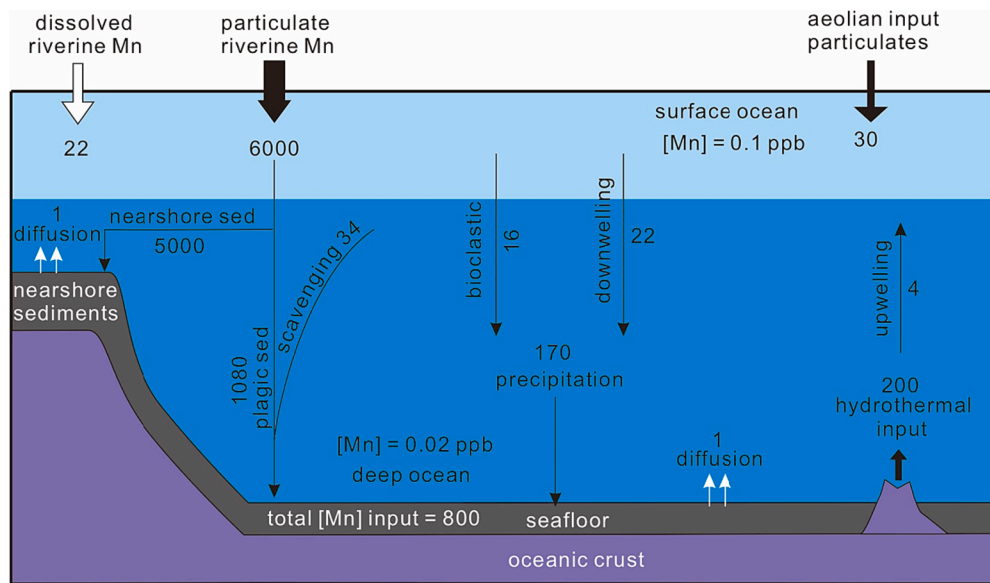
Fig. 10. The modern marine Mn cycle. Numeric values are estimated fluxes in units of $\mu g\ cm^{-2}\ 10^{-3}\ yr^{-1}$ (except for labeled concentrations in units of ppb) (modified from Bender et al., 1977; McLennan and Murray, 1999).

in Wu et al., 2016). Submarine volcanic debris and associated volca-nogenic structures are frequently present within the manganese-rich interval, and the close relationship between manganese abundance and these features reflects the influence of hydrothermal activity (Zhou et al., 2013; Kuang et al., 2014). Fault zones are commonly character-ized by high fluxes of Mn^{2+} related to hydrothermal emissions and submarine volcanism (Kearey et al., 2009; Zhou et al., 2022), and the fault zones bounding the horsts and grabens of the Nanhua Basin are known to have been intermittently active from the Late Neoproterozoic through the Early Paleozoic (Charvet, 2013; Yao et al., 2014). All these considerations signify a close relationship between fault zones and hy-drothermal venting in the Cryogenian Nanhua Basin.

Petrographic observations and Raman analysis provide further evi-dence of the link between hydrothermalism and Mn-carbonate precipi-tation (Fig. 3). Sample LB-304 records a mm-scale alternation of kutnohorite and Ca-rhodochrosite laminae. Although both minerals require elevated aqueous Mn concentrations, Ca-rhodochrosite $[Mn_xCa_{1-x}(CO_3)$, where x is typically > 0.9] requires higher aqueous Mn^{2+}/Ca^{2+} ratios than kutnohorite $[CaMn(CO_3)_2]$ (Gao et al., 2021). Since Mn^{2+} levels were controlled by vent emissions, the alternating precipitation of Ca-rhodochrosite and kutnohorite laminae is likely to record the episodicity of hydrothermal activity in the deep Nanhua Basin. This inference is consistent with the relationship between hy-drothermal proxies and Mn-carbonate intervals (Fig. 10), and further supported by the significant correlation between Mn and hydrothermal proxies (Eu/Eu*$_{SN}$, $r = +0.64$; $p(\alpha) < 0.01$; $\varepsilon Nd_{(660\ Ma)}$, $r = -0.64$; $p(\alpha) < 0.01$) (Fig. S2). The strong correlation between hydrothermal proxies and B/Ga, indicating hydrothermal fluid influx may have regulated water column salinity (Fig. 11), through which the precipitation of Mn-carbonate was affected as well. The close relationship between hydro-thermal activities and precipitation of Mn-carbonate holds regardless of whether Mn-carbonate formation proceeded via the "diagenetic model" (Yu et al., 2016, 2019) or the "direct precipitation model" (Wittkop et al., 2020).

Based on geological settings and controls on sedimentary Mn enrichment, the Red Sea represents an appropriate modern analog for the post-Sturtian Nanhua Basin. The Red Sea is a narrow ocean basin formed by rifting of the Arabian and African plates, which opened during the Oligocene (~30–20 Ma) (Wilson, 1963; Khalil and McClay et al., 2001; Rasul et al., 2015). It features massive hydrothermal activity and large-scale iron-manganese oxyhydroxide precipitation (Taitel-
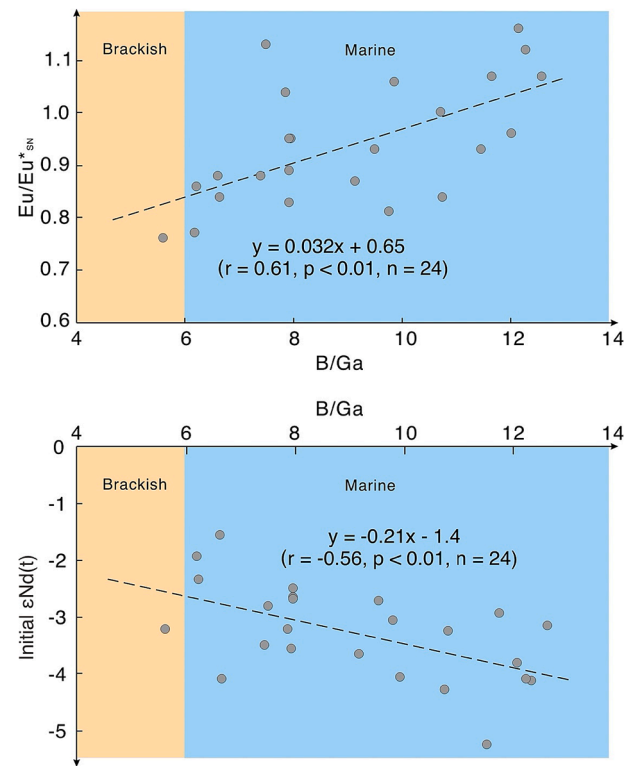

Fig. 11. B/Ga versus (A) Eu/Eu*$_{SN}$ and (B) initial $\varepsilon Nd(t)$ versus B/Ga for drillcore ZK4207.

Goldman et al., 2009). Influx of hydrothermal brines provides signifi-cant amounts of Mn^{2+} and nutrients to the basin, which subsequently stimulate primary production and microbial activity (Boyd and Ellwood, 2010; Resing et al., 2015). The high salinity of its deep watermass results from discharge of hot, high-salinity brines, promoting a stratified water column (Blanc and Anschutz, 1995; Laurila et al., 2015). Mn^{2+} is oxidized to $nMnO_2 \cdot mH_2O$ and forms todorokite in the alkaline surface layer in which oxygen levels are high, while manganite forms in the oxygen-deficient and low-pH deep layer (Butuzova et al., 1990; Scholten

et al., 2017). Differences in the Mn-mineral types of the Red Sea (i.e., todorokite and manganite) (Butuzova et al., 1990) versus the Nanhua Basin (i.e., rhodochrosite) may be due to unique aspects of their watermass chemistry, e.g., the Red Sea features relatively higher oxygen levels and dissolved Fe/Mn ratios (Butuzova et al., 1990; Roik et al., 2018) than the Cryogenian Nanhua Basin. Nonetheless, similarities in tectonic environment, fault-related hydrothermal activity, and paleoenvironmental boundary conditions between the modern Red Sea and Cryogenian Nanhua Basin suggest that rifting and associated hydrothermalism are commonly key factors in the development of massive Mn-ore deposits (Balkhanov and Razvalyayev, 1981; Zhou et al., 2013; Wu et al., 2016).

5.6. Microbial catalysis of Mn-carbonate precipitation

Microbial activity is widely regarded as playing a fundamental role in the formation of Mn-ore deposits, being a key feature of the "diagenetic model" (Tazaki, 2000; Polgári et al., 2012b, 2016; Biondi and Lopez, 2017; Yu et al., 2019; Huang et al., 2022). Bacterially mediated reduction of Mn(IV) and/or Mn(III) coupled to the oxidation of organic matter (into HCO_3^-) and the formation of Mn-carbonate minerals (rhodochrosite, kutnohorite) has been documented for various Mn-ore deposits (e.g., Okita et al., 1988; Polgári et al., 2012b, 2016; Yu et al., 2016; Dong et al., 2023). The enzymatic oxidation of Mn(II) to Mn(IV) by microbes is a common process in natural environments as well, with reported microbial precipitates including Mn minerals of almost every possible valence state (Ferris et al., 1987; Adams and Ghiorse, 1988; Mandernack and Tebo, 1993). The oxidation of manganese can in turn fuel the growth of chemolithoautotrophic microorganisms (Yu and Leadbetter, 2020). Aerobic Mn(II)-oxidizing bacteria typically inhabit environments proximal to hydrothermal settings, and catalyze the oxidation of Mn(II) with O_2 under a wide range of temperature conditions and Mn concentrations (Mandernack et al., 1995; Bargar et al., 2009; Wang et al., 2023). Ancient Mn deposits that exhibit microbially mediated metallogenic mechanisms range in age from Precambrian to Mesozoic (Mita and Miura, 2003; Polgári et al., 2012b; Planavsky et al., 2013; Biondi and Lopez, 2017; Daye et al., 2019; Yu et al., 2019; Yu and Leadbetter, 2020; Biondi et al., 2020; Huang et al., 2022; Dong et al., 2023), suggesting an antiquity to the role of microbes in the metallogenesis of Mn-ore deposits; this process requires free O_2 so Mn(II) oxidation is often directly linked to the origin of cyanobacteria (Planavsky et al., 2013). Dissolved Mn^{2+} may also be oxidized through biogeochemical pathways, including homogeneous photochemical, and enzymatically mediated electron-transfer process, in low-oxygen environments (Tebo and Emerson, 1985; Van Cappellen et al., 1998; Tebo et al., 2004, 2007; Liu et al., 2020).

One consequence stemming from high primary productivity levels and associated organic matter sinking fluxes during the post-Sturtian interglaciation is that the sediment surface in the Nanhua Basin would have promoted microbial activity and hence precipitation of Mn-carbonates through the "diagenetic model", which involves anaerobic microbial Mn(IV) reduction (Yu et al., 2019). In anoxic deep waters, these Mn(IV)-reducing bacteria may use Mn(IV) as an electron acceptor to mediate the oxidation of organic electron donors (e.g. Vandieken et al., 2012, 2014; Wang et al., 2022). Indeed, it has been proposed that this was likely a common scenario in post-Sturtian marginal-marine basins (Pruss et al., 2010; Bosak et al., 2011).

Biophysical interactions between microbial mats and the underlying sediments may have produced the microbially induced sedimentary structures that widely characterize this period and that provide important biosignatures for ancient microbial communities (Polgári et al., 2012a). It is not impossible that mineralized biomats are what we observe in thin sections of the 1st Member of the Datangpo Formation under low magnification (Fig. 2A-C), but as discussed above, it would not be clear what metabolism was being used given the bottom waters were anoxic. Under higher magnification, what appears to be bacterial

structures and a fabric-like lacework texture within the clay and Mn-carbonate matrix become visible (Fig. 2D-G). Unlike the concept of a biomat, these bacterial structures could simply be the fossilized remnants of sedimentary heterotrophs that oxidized accumulated planktonic biomass that settled out from the upper water column. Interestingly, in situ micro-Raman spectroscopy of sample LB-304 revealed a cyclic alternation of Ca-rhodochrosite, kutnohorite, and quartz laminae. These features are analogous to those in the Jurassic Úrkút Mn-carbonate deposit in Hungary, in which fossilized Mn-reducing heterotrophic bacteria are present (Polgári et al., 2012a). Mn (II) generated by those bacteria was subsequently oxidized via a microbial enzymatic reaction in a dysoxic environment at the sediment-–water interface, resulting in accumulation of fine-grained Mn(IV) oxides that were later transformed to Ca-rhodochrosite via microbial processes within the sediment (Polgári et al., 1991, 2012b). In this process, metals are typically electrostatically bound to the anionic cell wall and surrounding extracellular polymeric substances, and these areas then act as nucleation sites for crystal growth (Konhauser, 1998). What is different in the present study units is that mineralization was likely the result of Mn(IV) reduction in an anoxic setting, with subsequent nucleation and growth of Mn-carbonates. This process accounts for the commonly observed mineralization of microbial fossils visible in thin sections in areas adjacent to Mn-carbonate minerals (Fig. 2). We therefore infer that Mn-carbonates in the Cryogenian Nanhua Basin formed mainly through diagenetic processes, although direct precipitation of some fraction of these Mn-carbonates cannot be completely discounted. A diagenetic origin for the Mn-ore deposits is further supported by the $\delta^{13}C_{carb}$ proxy, which shows a significant negative correlation with Mn content ($r = -0.61$, $n = 14$; $p(\alpha) < 0.05$) as well as extremely low values in the HBI (ca. –7 to –6 ‰) (Fig. 4).

5.7. Salinity-based model of manganese enrichment for ore deposits in Nanhua Basin

Based on the foregoing analysis, we propose an integrated model to account for the watermass salinity, paleoenvironmental conditions, Mn sources, and microbial processes that led to formation of Mn-carbonate ores in the 1st Member of the Cryogenian Datangpo Formation. In this model, salinity variation plays a fundamental role, as indicated by the strong correlation between Mn content and B/Ga ($r = +0.59$; $p(\alpha) < 0.0001$; Fig. 12). Salinity variation in the Nanhua Basin was due to glacial meltwater runoff to its surface layer during the Sturtian deglaciation combined with hydrothermal inputs to its deep layer, producing a strongly stratified water column characterized by an oxygen-depleted and ferruginous deep watermass. In this context, hydrothermal activity provided large amounts of Mn^{2+} that were upwelled into shallow oxic waters where it was then oxidized to Mn(IV) by some of the bacterial
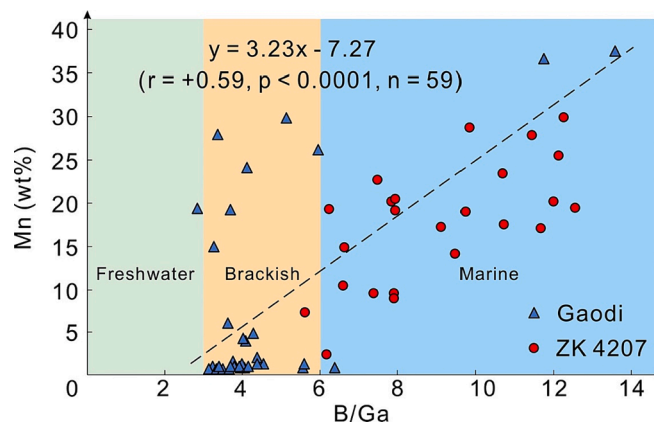

Fig. 12. Mn versus salinity proxy B/Ga for the study interval in drillcore ZK4207 and Gaodi Section (Cheng et al., 2021).

constituents in the planktonic community. Then, the MnO_2 and dead cells settled to the seafloor where the organic material accumulated into what is now visible as the organic laminae. With the MnO_2 and biomass now in anoxic sediments, dissimilatory Mn(IV) reduction subsequently produced Mn(II), allowing large-scale Mn-carbonate precipitation (Fig. 13A). During intervals of weaker hydrothermal activity, the deep watermass was characterized by lower salinity, reduced Mn^{2+} levels, euxinic conditions, more limited organic matter sinking fluxes and reduced microbial activity, favoring Mn-shale accumulation over Mn-carbonate production (Fig. 13B).

Peak hydrothermal activity occurred during deposition of the Middle Unit (the "high-boron interval" or HBI of Yu et al., 2022), characterized by relatively higher productivity and more reducing conditions (Figs. 3, 4). As discussed above, enhanced nutrient inputs from massive hydrothermal discharge stimulated primary productivity and promoted organic carbon sinking fluxes, which yielded porewater HCO_3^- during remineralization of organic matter. This additional alkalinity generated

conditions favorable for the precipitation of Mn-carbonates. The covariation of these paleoenvironmental conditions (paleosalinity, redox condition, hydrothermal activities) with the precipitation of Mn-carbonate is most readily observed at the basal (899.2–901.3 m) and HBI (891–896 m) intervals of the Datangpo Formation (Figs. 3, 4). The intimate relationship between watermass salinity and Mn enrichment is further supported by their similar vertical trends (Fig. 4) and significant positive correlations of Mn content with the salinity proxy B/Ga ($r = +0.59$; $p(\alpha) < 0.01$) (Fig. 12). Collectively, these observations establish an intimate relationship between the megallogenesis of Mn-ore deposits and watermass salinity.

6. Conclusions

Here, we present an integrated study of the petrology, major and trace elements, and isotope geochemistry of Mn-carbonates from the 1st Member of the Cryogenian Datangpo Formation in the Nanhua Basin,
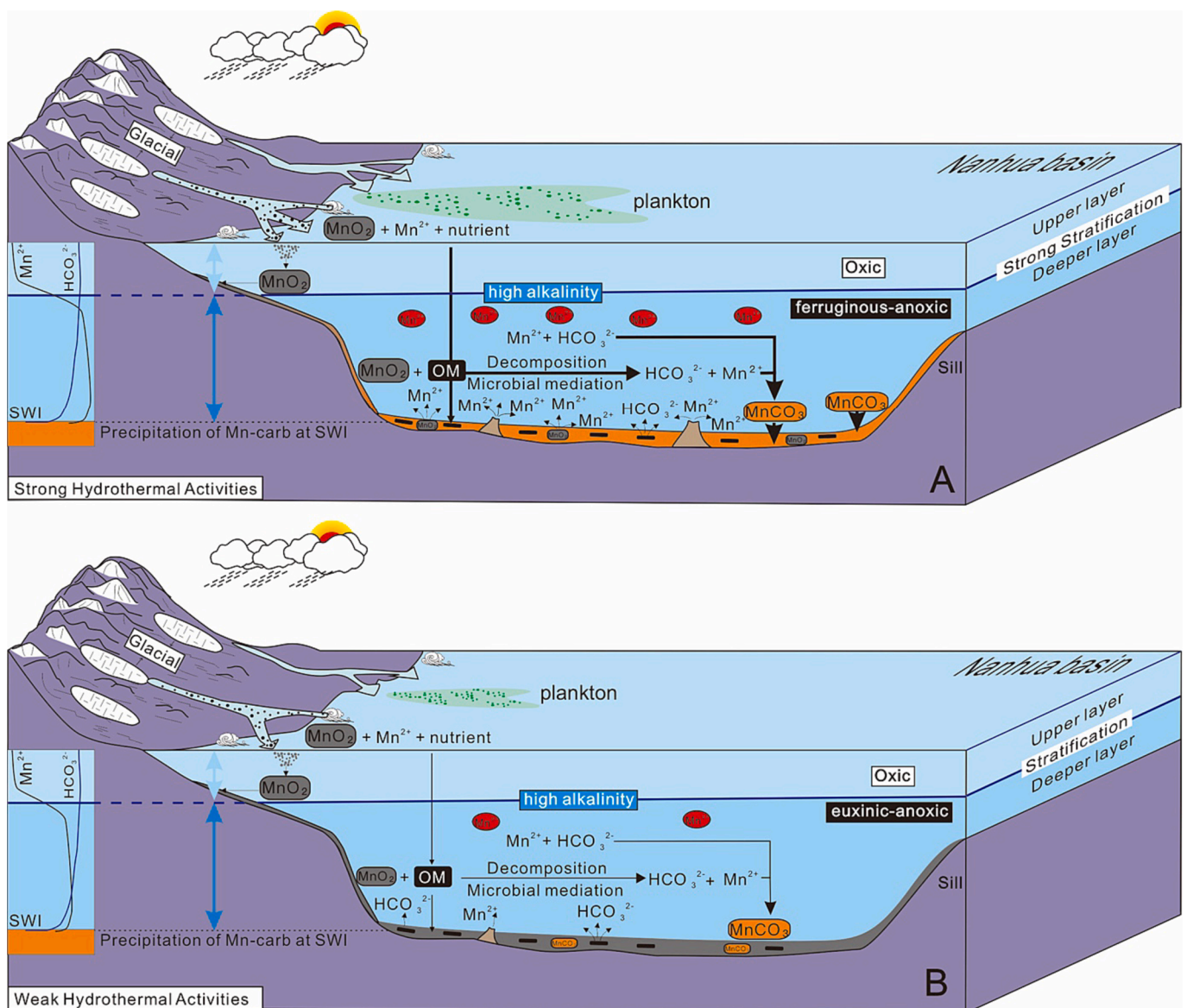

Fig. 13. Depositional model for the metallogenesis of Mn-carbonates in the Datangpo Formation, Nanhua Basin, China. SWI: the sediment–water interface. (A) Strong hydrothermal activity: the basin was characterized by higher Mn levels, stronger water column stratification, higher primary productivity and OM fluxes, enhancing precipitation of $MnCO_3$. (B) Weak hydrothermal activity: the basin was characterized by lower Mn levels, weaker water column stratification, lower primary productivity and OM fluxes, and reduced precipitation of $MnCO_3$. The relative ratio of Mn to alkalinity (HCO_3^-) is higher in A than in B, with vertical variation of Mn and HCO_3^- levels presented as profiles on the left side of the block diagrams.

China. Results indicate that abundant Mn^{2+} in Cryogenian Basin was sourced mainly from hydrothermal emissions, which also led to a rise in watermass salinity. The rise of watermass salinity promoted the stratification of the water column and supported the development of a ferruginous anoxic deep watermass. Extra nutrients related to hydrothermal emissions stimulated primary microbial productivity in the water column (e.g., Mn(II) oxidation). Enhanced water-column stratification promoted organic matter sinking fluxes that, in turn, fueled dissimilatory Mn(IV) reduction, which in turn, produced additional porewater alkalinity and Mn^{2+}. These changes collectively established conditions favorable for Mn-carbonate precipitation. Evidence of microbial activity in thin sections indicates the critical role of heterochemotrophic microbes in the reduction of Mn(IV) and the formation of Mn-carbonate deposits in the Nanhua Basin, similar to the Úrkút Mn-carbonate deposits in Hungary.

The salinity-based Mn-carbonate model established in the present study may serve as a counterpart to the alkalinity model of Yu et al. (2022), with these two models jointly providing a comprehensive understanding of the metallogenesis of the Datangpo Mn-ore deposits. Reconstructed salinity-based watermass conditions and formation pathways for the Mn-carbonates of the Cryogenian Nanhua Basin established here may further provide insights into the paleoenvironmental conditions required for generation of massive Mn-carbonate deposits formed in other epeiric sea settings.

CRediT authorship contribution statement

Wei Wei: Conceptualization, Writing – original draft, Writing – review & editing. **Wenchao Yu:** Supervision, Writing – review & editing. **Yuansheng Du:** Funding acquisition, Resources, Supervision. **Thomas J. Algeo:** Conceptualization, Writing – review & editing. **Zhiquan Li:** Writing – review & editing. **Meng Cheng:** Writing – review & editing. **Ping Wang:** Writing – review & editing. **Jingyu Zhang:** Writing – review & editing. **Leslie J. Robbins:** Writing – review & editing. **Kurt Konhauser:** Conceptualization, Writing – review & editing.

Declaration of competing interest

The authors declare that they have no known competing financial interests or personal relationships that could have appeared to influence the work reported in this paper.

Data availability

Data will be made available on request.

Acknowledgments

Appendix A. Supplementary material

Supplementary data to this article can be found online at https://doi.org/10.1016/j.precamres.2024.107309.

References

Adams, L.F., Ghiorse, W.C., 1988. Oxidation state of Mn in the Mn oxide produced by *Leptothrix discophora* SS-1. Geochim. Cosmochim. Acta 52 (8), 2073–2076.

Ai, J., Zhong, N., Zhang, T., Zhang, Y., Wang, T., George, S.C., 2021. Oceanic water chemistry evolution and its implications for post-glacial black shale formation: Insights from the Cryogenian Datangpo Formation. South China. Chemical Geology 566, 120083.

Algeo, T. J., Heckel, P. H., Maynard, J. B., Blakey, R., & Rowe, H. (2008). Modern and ancient epeiric seas and the super-estuarine circulation model of marine anoxia. In: Pratt, B. & Holmden, C. (eds.), Dynamics of Epeiric Seas: Sedimentological, Paleontological and Geochemical Perspectives. St. John's, Canada: Geological Association of Canada, Special Publication 48, 7-38.

Algeo, T.J., Ingall, E., 2007. Sedimentary Corg: P ratios, paleocean ventilation, and Phanerozoic atmospheric pO2. Palaeogeogr. Palaeoclimatol. Palaeoecol. 256 (3–4), 130–155.

Algeo, T.J., Liu, J., 2020. A re-assessment of elemental proxies for paleoredox analysis. Chem. Geol. 540, 119549.

Algeo, T.J., Maynard, J.B., 2008. Trace-metal covariation as a guide to water-mass conditions in ancient anoxic marine environments. Geosphere 4 (5), 872–887.

Algeo, T.J., Henderson, C.M., Tong, J., Feng, Q., Yin, H., Tyson, R.V., 2013. Plankton and productivity during the Permian-Triassic boundary crisis: an analysis of organic carbon fluxes. Global Planet. Change 105, 52–67.

Anadón, P., Gliozzi, E., & Mazzini, I. (2002). Paleoenvironmental reconstruction of marginal marine environments from combined paleoecological and geochemical analyses on ostracods. In: Holmes, J.A., Chivas, A.R. (eds.), The Ostracoda: Applications in Quaternary Research, American Geophysical Union, Geophysical Monograph 131, pp. 227-247.

Balkhanov, V.V., Razvalyayev, A.V., 1981. The origin of the manganese deposits of the western shore of the Red Sea (in association with rifting). Int. Geol. Rev. 23 (2), 162–166.

Bau, M., Dulski, P., 1996. Distribution of yttrium and rare-earth elements in the Penge and Kuruman iron-formations, Transvaal Supergroup. South Africa. Precambrian Research 79 (1–2), 37–55.

Bazilevskaya, E.S., 2006. Sources of manganese deposited as oceanic Fe-Mn ore. Geol. Ore Deposits 48 (2), 134–143.

Bender, M.L., Klinkhammer, G.P., Spencer, D.W., 1977. Manganese in seawater and the marine manganese balance. Deep-Sea Res. 24 (9), 799–812.

Biondi, J.C., Lopez, M., 2017. Urucum Neoproterozoic-Cambrian manganese deposits (MS, Brazil): Biogenic participation in the ore genesis, geology, geochemistry, and depositional environment. Ore Geol. Rev. 91, 335–386.

Biondi, J.C., Polgári, M., Gyollai, I., Fintor, K., Kovács, I., Fekete, J., Mojzsis, S.J., 2020. Biogenesis of the Neoproterozoic kremydilite manganese ores from Urucum (Brazil)– A new manganese ore type. Precambr. Res. 340, 105624.

Blanc, G., Anschutz, P., 1995. New stratification in the hydrothermal brine system of the Atlantis II Deep. Red Sea. Geology 23 (6), 543–546.

Bosak, T., Lahr, D.J.G., Pruss, S.B., Macdonald, F.A., Dalton, L., Matys, E., 2011. Agglutinated tests in post-Sturtian cap carbonates of Namibia and Mongolia. Earth Planet. Sci. Lett. 308 (1–2), 29–40.

Boström, K., 1983. Genesis of ferromanganese deposits—Diagnostic criteria for recent and old deposits. In: Rona, P.A. (Ed.), Hydrothermal Processes at Seafloor Spreading Centers. Springer, Berlin, pp. 473–489.

Boyd, P.W., Ellwood, M.J., 2010. The biogeochemical cycle of iron in the ocean. Nat. Geosci. 3 (10), 675–682.

Brocks, J.J., Jarrett, A.J., Sirantoine, E., Hallmann, C., Hoshino, Y., Liyanage, T., 2017. The rise of algae in Cryogenian oceans and the emergence of animals. Nature 548 (7669), 578–581.

Burdige, D.J., 2007. Preservation of organic matter in marine sediments: controls, mechanisms, and an imbalance in sediment organic carbon budgets? Chem. Rev. 107, 467–485.

Butuzova, G.Y., Drits, V.A., Morozov, A.A., Gorschkov, A.I., 1990. In: Processes of Formation of Iron—Manganese Oxyhydroxides in the Atlantis-II and Thetis Deeps of the Red Sea. Blackwell Publishing Ltd., Oxford, UK, pp. 57–72.

Camprubí, A., Canet, C., Rodríguez-Díaz, A.A., Prol-Ledesma, R.M., Blanco-Florido, D., Villanueva, R.E., López-Sánchez, A., 2008. Geology, ore deposits and hydrothermal venting in Bahía Concepción, Baja California Sur. Mexico. Island Arc 17 (1), 6–25.

Charvet, J., 2013. The Neoproterozoic–early Paleozoic tectonic evolution of the South China Block: an overview. J. Asian Earth Sci. 74, 198–209.

Chen, D.F., Chen, X.P., 1992. Geological and geochemical characteristics of Songtao hydrothermal sedimentary manganese deposit. Guizhou. Acta Sedimentologica Sinica 10 (4), 35–43 in Chinese with English abstract.

Cheng, M., Zhang, Z., Algeo, T.J., Liu, S., Liu, X., Wang, H., Chang, B., Jin, C., Pan, W., Cao, M., Li, C., 2021. Hydrological controls on marine chemistry in the Cryogenian Nanhua Basin (South China). Earth Sci. Rev. 218, 103678.

Cheng, M., Zhang, Z., Jin, C., Wei, W., Wang, H., Algeo, T.J., Li, C., 2023. Salinity variation and hydrographic dynamics in the early Cambrian Nanhua Basin (South China). Sci. China Earth Sci. 1–11.

Cox, G.M., Halverson, G.P., Stevenson, R.K., Vokaty, M., Poirier, A., Kunzmann, M., Li, Z. X., Denyszyn, S.W., Strauss, J.V., Macdonald, F.A., 2016. Continental flood basalt weathering as a trigger for Neoproterozoic Snowball Earth. Earth Planet. Sci. Lett. 446, 89–99.

Daye, M., Klepac-Ceraj, V., Pajusalu, M., Rowland, S., Farrell-Sherman, A., Beukes, N., Tamura, N., Fournier., G., and Bosak, T., 2019. Light-driven anaerobic microbial oxidation of manganese. Nature 576 (7786), 311–314.

Delacour, A., Früh-Green, G.L., Frank, M., Gutjahr, M., Kelley, D.S., 2008. Sr-and Nd-isotope geochemistry of the Atlantis Massif (30°N, MAR): implications for fluid fluxes and lithospheric heterogeneity. Chem. Geol. 254 (1–2), 19–35.

Dellwig, O., Schnetger, B., Brumsack, H.J., Grossart, H.P., Umlauf, L., 2012. Dissolved reactive manganese at pelagic redoxclines (part II): Hydrodynamic conditions for accumulation. J. Mar. Syst. 90 (1), 31–41.

DePaolo, D.J., Wasserburg, G.J., 1979. Petrogenetic mixing models and Nd-Sr isotopic patterns. Geochim. Cosmochim. Acta 43 (4), 615–627.

Dierssen, H. M., Smith, R. C., & Vernet, M. (2002). Glacial meltwater dynamics in coastal waters west of the Antarctic peninsula. Proceedings of the National Academy of Sciences (U.S.A.), 99(4), 1790-1795.

Dong, Z.G., Peng, Z.D., Robbins, L.J., Konhauser, K.O., Zhang, B.L., Zhang, L.C., Li, J., Li, W.J., Zhang, L., Wang, C.L., 2023. Episodic ventilation of euxinic bottom waters triggers the formation of black shale-hosted Mn carbonate deposits. Geochim. Cosmochim. Acta 341, 132–149.

Falkowski, P.G., Barber, R.T., Smetacek, V., 1998. Biogeochemical controls and feedbacks on ocean primary production. Science 281 (5374), 200–206.

Fan, D.L., Liu, T., Ye, J., 1992. The process of formation of manganese carbonate deposits hosted in black shale series. Econ. Geol. 87 (5), 1419–1429.

Ferris, F.G., Fyfe, W.S., Beveridge, T.J., 1987. Manganese oxide deposition in a hot spring microbial mat. Geomicrobiol J. 5 (1), 33–42.

Feulner, G., Hallmann, C., Kienert, H., 2015. Snowball cooling after algal rise. Nat. Geosci. 8 (9), 659–662.

Frakes, L., Bolton, B.R., 1992. Effects of ocean chemistry, sea level, and climate on the formation of primary sedimentary manganese ore deposits. Econ. Geol. 87 (5), 1207–1217.

Freitas, B.T., Rudnitzki, I.D., Morais, L., Campos, M.D.R., Almeida, R.P., Warren, L.V., Boggiani, P.C., Caetano-Filho, S., Bedoya-Rueda, C., Babinski, M., Fairchild, T.R., 2021. Cryogenian glaciostatic and eustatic fluctuations and massive Marinoan-related deposition of Fe and Mn in the Urucum District. Brazil. Geology 49 (12), 1478–1483.

Frieling, J., Svensen, H. H., Planke, S., Cramwinckel, M. J., Selnes, H., & Sluijs, A. (2016). Thermogenic methane release as a cause for the long duration of the PETM. Proceedings of the National Academy of Sciences (U.S.A.), 113(43), 12059-12064.

Gao, Z., Zhu, X., Wang, D., Pan, C., Yan, B., Li, J., 2021. Insights into hydrothermal controls and processes leading to the formation of the Late Ediacaran Gaoyan stratiform manganese-carbonate deposit. Southwest China. Ore Geology Reviews 139, 104524.

Gilleaudeau, G.J., Algeo, T.J., Lyons, T.W., Bates, S., Anbar, A.D., 2021. Novel watermass reconstruction in the Early Mississippian Appalachian Seaway based on integrated proxy records of redox and salinity. Earth Planet. Sci. Lett. 558, 116746.

Glasby, G.P., 1988. Manganese deposition through geological time: dominance of the post-Eocene deep-sea environment. Ore Geol. Rev. 4 (1–2), 135–143.

Goddéris, Y., Donnadieu, Y., Nédélec, A., Dupré, B., Dessert, C., Grard, A., Ramstein, G., François, L.M., 2003. The Sturtian 'snowball' glaciation: fire and ice. Earth Planet. Sci. Lett. 211 (1–2), 1–12.

Goddéris, Y., Donnadieu, Y., Dessert, C., Dupré, B., Fluteau, F., François, L.M., Meert, J., Nédélec, A., Ramstein, G., 2007. Coupled modeling of global carbon cycle and climate in the Neoproterozoic: links between Rodinia breakup and major glaciations. C. R. Geosci. 339 (3–4), 212–222.

Gomez-Saez, G.V., Pop Ristova, P., Sievert, S.M., Elvert, M., Hinrichs, K.U., Bühring, S.I., 2017. Relative importance of chemoautotrophy for primary production in a light exposed marine shallow hydrothermal system. Front. Microbiol. 8, 702.

Guieu, C., Duce, R., Arimoto, R., 1994. Dissolved input of manganese to the ocean: Aerosol source. J. Geophys. Res. Atmos. 99 (D9), 18789–18800.

Gutzmer, J., Beukes, N.J., 1998. The manganese formation of the Neoproterozoic Penganga Group, India; revision of an enigma. Econ. Geol. 93 (7), 1091–1102.

Häusler, K., Dellwig, O., Schnetger, B., Feldens, P., Leipe, T., Moros, M., Pollehnea, F., Schönkea, M., Wegwertha, A., Arz, H.W., 2018. Massive Mn carbonate formation in the Landsort Deep (Baltic Sea): Hydrographic conditions, temporal succession, and Mn budget calculations. Mar. Geol. 395, 260–270.

Hayes, J.M., Strauss, H., Kaufman, A.J., 1999. The abundance of ^{13}C in marine organic matter and isotopic fractionation in the global biogeochemical cycle of carbon during the past 800 Ma. Chem. Geol. 161 (1–3), 103–125.

He, Z.W., Yang, R.D., Gao, J.B., Cheng, W., Liu, S., Zhang, W.F., 2014. The geochemical characteristics and sedimentary environment of manganese-bearing rock series of Daotuo manganese deposit, Songtao County of Guizhou Province. Geol. Rev. 60 (5), 1061–1075 in Chinese with English abstract.

Herndon, E.M., Havig, J.R., Singer, D.M., McCormick, M.L., Kump, L.R., 2018. Manganese and iron geochemistry in sediments underlying the redox-stratified Fayetteville Green Lake. Geochim. Cosmochim. Acta 231, 50–63.

Hoffman, P.F., Schrag, D.P., 2002. The snowball Earth hypothesis: testing the limits of global change. Terra Nova 14 (3), 129–155.

Hoffman, P.F., 26 co-authors,, 2017. Snowball Earth climate dynamics and Cryogenian geology-geobiology. Sci. Adv. 3, e1600983.

Huang, Q., Pi, D.-H., Jiang, S.-Y., Liu, D., Yan, H., Mänd, K., Kirsimäe, K., Bishop, B., Robbins, L.J., Yang, S.-S., 2022. The dual role of microbes in the formation of the Malkantu manganese carbonate deposit, NW China: Petrographic, geochemical, and experimental evidence. Chem Geol 606, 120992. https://doi.org/10.1016/j.chemgeo.2022.120992.

Hulten, M.V., Middag, R., Dutay, J.C., Baar, H.D., Roy-Barman, M., Gehlen, M., Tagliabue, A., Sterl, A., 2017. Manganese in the west Atlantic Ocean in the context of the first global ocean circulation model of manganese. Biogeosciences 14 (5), 1123–1152.

Humphris, S.E., Bach, W., 2005. On the Sr isotope and REE compositions of anhydrites from the TAG seafloor hydrothermal system. Geochim. Cosmochim. Acta 69 (6), 1511–1525.

Jenkyns, H.C., 2010. Geochemistry of oceanic anoxic events. Geochem. Geophys. Geosyst. 11 (3).

Johnston, D.T., Macdonald, F.A., Gill, B.C., Hoffman, P.F., Schrag, D.P., 2012. Uncovering the Neoproterozoic carbon cycle. Nature 483 (7389), 320–323.

Kearey, P., Klepeis, K.A., Vine, F.J., 2009. Global Tectonics. John Wiley & Sons 463 pp.

Konhauser, K.O., 1998. Diversity of bacterial iron mineralization. Earth Sci. Rev. 43 (3–4), 91–121.

Kraal, P., Slomp, C.P., Forster, A., Kuypers, M.M., 2010. Phosphorus cycling from the margin to abyssal depths in the proto-Atlantic during oceanic anoxic event 2. Palaeogeogr. Palaeoclimatol. Palaeoecol. 295 (1–2), 42–54.

Kuang, W.L., Li, X.Y., Yang, S.X., 2014. The mineralization geological characteristics and genesis of Minle type manganese deposit in northwestern of Hunan Province. Chinese Journal of Geology 49 (1), 305–323 in Chinese with English abstract.

Lansard, B., Mucci, A., Miller, L.A., Macdonald, R.W., Gratton, Y., 2012. Seasonal variability of water mass distribution in the southeastern Beaufort Sea determined by total alkalinity and δ^{18}O. J. Geophys. Res. Oceans 117 (C3).

Laurila, T.E., Hannington, M.D., Leybourne, M., Petersen, S., Devey, C.W., Garbe-Schönberg, D., 2015. New insights into the mineralogy of the Atlantis II Deep metalliferous sediments, Red Sea. Geochem. Geophys. Geosyst. 16 (12), 4449–4478.

Li, Z.X., Bogdanova, S., Collins, A.S., Davidson, A., De Waele, B., Ernst, R.E., Fitzsimons, I.C.W., Fuck, R.A., Gladkochub, D.P., Jacobs, J., Karlstrom, K.E., 2008. Assembly, configuration, and break-up history of Rodinia: a synthesis. Precambr. Res. 160 (1–2), 179–210.

Li, Z.H., Evans, D.A.D., Halverson, G.P., 2013. Neoproterozoic glaciations in a revised global palaeogeography from the breakup of Rodinia to the assembly of Gondwanaland. Sed. Geol. 294, 219–232.

Li, X.H., Li, W.X., Li, Z.X., Lo, C.H., Wang, J., Ye, M.F., Yang, Y.H., 2009. Amalgamation between the Yangtze and Cathaysia Blocks in South China: constraints from SHRIMP U-Pb zircon ages, geochemistry and Nd–Hf isotopes of the Shuangxiwu volcanic rocks. Precambr. Res. 174 (1–2), 117–128.

Li, C., Love, G.D., Lyons, T.W., Fike, D.A., Sessions, A., Chu, X.L., 2010. A stratified redox model for the Ediacaran ocean. Science 328, 80–83.

Li, C., Love, G.D., Lyons, T.W., Scott, C.T., Feng, L., Huang, J., Chang, H., Zhang, Q., Chu, X., 2012. Evidence for a redox stratified Cryogenian marine basin, Datangpo Formation, South China. Earth Planet. Sci. Lett. 331, 246–256.

Li, C., Shi, W., Cheng, M., Jin, C., Algeo, T.J., 2020. The redox structure of ediacaran and early Cambrian oceans and its controls. Sci. Bull. 65 (24), 2141–2149.

Little, S., Wood, P.J., Elliott, M., 2017. Quantifying salinity-induced changes on estuarine benthic fauna: The potential implications of climate change. Estuar. Coast. Shelf Sci. 198, 610–625.

Liu, W., Hao, J., Elzinga, E. J., Piotrowiak, P., Nanda, V., Yee, N., & Falkowski, P. G. (2020). Anoxic photogeochemical oxidation of manganese carbonate yields manganese oxide. Proceedings of the National Academy of Sciences (U.S.A.), 117 (37), 22698-22704.

Liu, Y., Li, C., Algeo, T.J., Fan, J., 2016. Global and regional controls on marine redox changes across the Ordovician-Silurian boundary in South China. Palaeogeogr. Palaeoclimatol. Palaeoecol. 463, 180–191.

Love, G.D., Grosjean, E., Stalvies, C., Fike, D.A., Grotzinger, J.P., Bradley, A.S., Kelly, A. E., Bhatia, M., Meredith, W., Snape, C.E., Bowring, S.A., Condon, D.J., Summons, R. E., 2009. Fossil steroids record the appearance of Demospongiae during the Cryogenian period. Nature 457 (7230), 718–721.

Lyons, T.W., Werne, J.P., Hollander, D.J., Murray, R.W., 2003. Contrasting sulfur geochemistry and Fe/Al and Mo/Al ratios across the last oxic-to-anoxic transition in the Cariaco Basin. Venezuela. Chem. Geol. 195, 131–157.

Ma, Z., Liu, X., Yu, W., Du, Y., Du, Q., 2019. Redox conditions and manganese metallogenesis in the Cryogenian Nanhua Basin: Insight from the basal Datangpo Formation of South China. Palaeogeogr. Palaeoclimatol. Palaeoecol. 529, 39–52.

Macdonald, F.A., Schmitz, M.D., Crowley, J.L., Roots, C.F., Jones, D.S., Maloof, A.C., Strauss, J.V., Cohen, P.A., Johnston, D.T., Schrag, D.P., 2010. Calibrating the Cryogenian. Science 327 (5970), 1241–1243.

Mandernack, K.W., Tebo, B.M., 1993. Manganese scavenging and oxidation at hydrothermal vents and in vent plumes. Geochim. Cosmochim. Acta 57 (16), 3907–3923.

Mandernack, K.W., Post, J., Tebo, B.M., 1995. Manganese mineral formation by bacterial spores of the marine Bacillus, strain SG-1: evidence for the direct oxidation of Mn(II) to Mn(IV). Geochim. Cosmochim. Acta 59 (21), 4393–4408.

Marchig, V., Gundlach, H., Möller, P., Schley, F., 1982. Some geochemical indicators for discrimination between diagenetic and hydrothermal metalliferous sediments. Mar. Geol. 50 (3), 241–256.

Maynard, J.B., 2010. The chemistry of manganese ores through time: a signal of increasing diversity of earth-surface environments. Econ. Geol. 105 (3), 535–552.

Maynard, J.B., Kuleshov, V., 2017. Chapter 4 - The major epochs and phases of manganese accumulation in the Earth's history. In: Geochemistry, I., Kuleshov, V. (Eds.), Isotope Geochemistry: the Origin and Formation of Manganese Rocks and Ores. Elsevier, Amsterdam, pp. 353–383.

McCollom, T.M., 2000. Geochemical constraints on primary productivity in submarine hydrothermal vent plumes. Deep Sea Res. Part I 47 (1), 85–101.

McLennan, S.M., Murray, R.W., 1999. Geochemistry of sediments. In: Marshall, C.P., Fairbridge, R.W. (Eds.), Encyclopedia of Geochemistry. Kluwer Academic Publishers, Dordrecht, pp. 282–292.

Mendez, J., Guieu, C., Adkins, J., 2010. Atmospheric input of manganese and iron to the ocean: Seawater dissolution experiments with Saharan and North American dusts. Mar. Chem. 120 (1–4), 34–43.

Merdith, A., Williams, S.E., Collins, A.S., Tetley, M.G., Mulder, J.A., Blades, M.L., Young, A., Armistead, S.E., Cannon, J., Zahirovic, S., Müller, R.D., 2021. Extending full-plate tectonic models into deep time: Linking the Neoproterozoic and the Phanerozoic. Earth Sci. Rev. 214, 103477.

Meyer, K.M., Yu, M., Lehrmann, D., van de Schootbrugge, B., Payne, J.L., 2013. Constraints on Early Triassic carbon cycle dynamics from paired organic and inorganic carbon isotope records. Earth Planet. Sci. Lett. 361, 429–435.

Middelburg, J. J. (2019). Marine Carbon Biogeochemistry: A Primer for Earth System Scientists, Springer Nature, 118 pp.

Mita, N., Miura, H., 2003. Evidence of microbial activity in the formation of manganese wads at the Asahidake hot spring in Hokkaido. Japan. Resource Geology 53 (3), 233–238.

Narejo, A.A., Shar, A.M., Fatima, N., Sohail, K., 2019. Geochemistry and origin of Mn deposits in the Bela ophiolite complex, Balochistan, Pakistan. J. Pet. Explor. Prod. Technol. 9 (4), 2543–2554.

Nettersheim, B.J., Brocks, J.J., Schwelm, A., Hope, J.M., Not, F., Lomas, M., Schmidt, C., Schiebel, R., Nowack, E.C., De Deckker, P., Pawlowski, J., 2019. Putative sponge biomarkers in unicellular Rhizaria question an early rise of animals. Nat. Ecol. Evol. 3 (4), 577–581.

Neumeister, S., Gratzer, R., Algeo, T.J., Bechtel, A., Gawlick, H.J., Newton, R.J., Sachsenhofer, R.F., 2015. Oceanic response to Pliensbachian and Toarcian magmatic events: implications from an organic-rich basinal succession in the NW Tethys. Global Planet. Change 126, 62–83.

Neumeister, S., Algeo, T.J., Bechtel, A., Gawlick, H.J., Gratzer, R., Sachsenhofer, R.F., 2016. Redox conditions and depositional environment of the Lower Jurassic Bächental bituminous marls (Tyrol, Austria). Austrian J. Earth Sci. 109 (2), 142–159.

Neumeister, S., Misch, D., Algeo, T.J., Gawlick, H.J., Gratzer, R., Sachsenhofer, R.F., 2020. Early diagenesis of organic-rich marls under shifting suboxic to euxinic conditions: The lower Toarcian of the Bächental basin. Mar. Pet. Geol. 120, 104513.

Noll Jr., P.D., Newsom, H.E., Leeman, W.P., Ryan, J.G., 1996. The role of hydrothermal fluids in the production of subduction zone magmas: evidence from siderophile and chalcophile trace elements and boron. Geochim. Cosmochim. Acta 60 (4), 587–611.

Okita, P.M., 1992. Manganese carbonate mineralization in the Molango District. Mexico. Economic Geology 87 (5), 1345–1366.

Okita, P.M., Maynard, J.B., Spiker, E.C., Force, E.R., 1988. Isotopic evidence for organic matter oxidation by manganese reduction in the formation of stratiform manganese carbonate ore. Geochim. Cosmochim. Acta 52 (11), 2679–2685.

Pan, W., Cao, M., Du, Y., Cheng, M., Zhou, Y.Q., Algeo, T.J., Zhao, M., Thibaulte, N., Li, C., Wei, G.Y., Dahl, T.W., 2021. Paired U and Mo isotope evidence for pervasive anoxia in the Cryogenian early interglacial ocean. Precambr. Res. 361, 106244.

Peng, X., Zhu, X.K., Shi, F., Yan, B., Zhang, F., Zhao, N., Peng, P., Li, J., Wang, D., Shields, G.A., 2019. A deep marine organic carbon reservoir in the non-glacial Cryogenian ocean (Nanhua Basin, South China) revealed by organic carbon isotopes. Precambr. Res. 321, 212–220.

Peter, J.M., Goodfellow, W.D., 1996. Mineralogy, bulk and rare earth element geochemistry of massive sulphide-associated hydrothermal sediments of the Brunswick Horizon, Bathurst Mining Camp, New Brunswick. Can. J. Earth Sci. 33, 252–283.

Pingitore Jr., N.E., Eastman, M.P., Sandidge, M., Oden, K., Freiha, B., 1988. The coprecipitation of manganese (II) with calcite: an experimental study. Mar. Chem. 25 (2), 107–120.

Pirajno, F., 2012. Hydrothermal Mineral Deposits: Principles and Fundamental Concepts for the Exploration Geologist. Springer, Berlin, p. 709.

Planavsky, N.J., Rouxel, O.J., Bekker, A., Lalonde, S.V., Konhauser, K.O., Reinhard, C.T., Lyons, T.W., 2010. The evolution of the marine phosphate reservoir. Nature 467 (7319), 1088–1090.

Polgári, M., Hein, J.R., Tóth, A.L., Pál-Molnár, E., Vigh, T., Bíró, L., Fintor, K., 2012a. Microbial action formed Jurassic Mn-carbonate ore deposit in only a few hundred years (Úrkút, Hungary). Geology 40 (10), 903–906.

Polgári, M., Hein, J.R., Vigh, T., Szabó-Drubina, M., Fórizs, I., Bíró, L., Müller, A., Tóth, A.L., 2012b. Microbial processes and the origin of the Úrkút manganese deposit, Hungary. Ore Geol. Rev. 47, 87–109.

Polgári, M., Hein, J.R., Bíró, L., Gyollai, I., Németh, T., Sajgó, C., Fekete, J., Schwark, L., Pál-Molnár, E., Hámor-Vidó, M., Vigh, T., 2016. Mineral and chemostratigraphy of a Toarcian black shale hosting Mn-carbonate microbialites (Úrkút, Hungary). Palaeogeogr. Palaeoclimatol. Palaeoecol. 459, 99–120.

Polgári, M., Gyollai, I., Fintor, K., Horváth, H., Pál-Molnár, E., Biondi, J.C., 2019. Microbially mediated ore-forming processes and cell mineralization. Front. Microbiol. 10, 2731.

Pruss, S.B., Bosak, T., Macdonald, F.A., McLane, M., Hoffman, P.F., 2010. Microbial facies in a Sturtian cap carbonate, the Rasthof Formation, Otavi Group, northern Namibia. Precambr. Res. 181 (1–4), 187–198.

Pu, J.P., Macdonald, F.A., Schmitz, M.D., Rainbird, R.H., Bleeker, W., Peak, B.A., Flowers, R.M., Hoffman, P.F., Rioux, M., Hamilton, M.A., 2022. Emplacement of the Franklin large igneous province and initiation of the Sturtian Snowball Earth. Science. Advances 8 (47), eadc9430.

Rasul, N., Stewart, I.C., Nawab, Z.A., 2015. Introduction to the Red Sea: its origin, structure, and environment. In: The Red Sea. Springer, Berlin, pp. 1–28.

Remírez, M.N., Algeo, T.J., 2020. Paleosalinity determination in ancient epicontinental seas: A case study of the T-OAE in the Cleveland Basin (UK). Earth Sci. Rev. 201, 103072.

Resing, J.A., Sedwick, P.N., German, C.R., Jenkins, W.J., Moffett, J.W., Sohst, B.M., Tagliabue, A., 2015. Basin-scale transport of hydrothermal dissolved metals across the South Pacific Ocean. Nature 523 (7559), 200–203.

Ridgwell, A.J., Kennedy, M.J., Caldeira, K., 2003. Carbonate deposition, climate stability, and Neoproterozoic ice ages. Science 302 (5646), 859–862.

Rio-Salas, D., Ochoa-Landín, L., Eastoe, C.J., Ruiz, J., Meza-Figueroa, D., Valencia-Moreno, M., Zúñiga-Hernández, H., Zúñiga-Hernández, L., Moreno-Rodríguez, V., Mendívil-Quijada, H., 2013. Genesis of manganese oxide mineralization in the Boleo region and Concepción Peninsula, Baja California Sur: constraints from Pb-Sr isotopes and REE geochemistry. Revista Mexicana De Ciencias Geológicas 30 (3), 482–499.

Roik, A., Röthig, T., Pogoreutz, C., Saderne, V., Voolstra, C.R., 2018. Coral reef carbonate budgets and ecological drivers in the central Red Sea–A naturally high temperature and high total alkalinity environment. Biogeosciences 15 (20), 6277–6296.

Rooney, A.D., Strauss, J.V., Brandon, A.D., Macdonald, F.A., 2015. A Cryogenian chronology: Two long-lasting synchronous Neoproterozoic glaciations. Geology 43 (5), 459–462.

Savenije, H.H.G., 2012. Salinity and Tides in Alluvial Estuaries, 2nd edn.,.

Schoepfer, S.D., Shen, J., Wei, H., Tyson, R.V., Ingall, E., Algeo, T.J., 2015. Total organic carbon, organic phosphorus, and biogenic barium fluxes as proxies for paleomarine productivity. Earth Sci. Rev. 149, 23–52.

Scholten, J.C., Staffers, P., Garbe-Schdönberg, D., Moammar, M., 2017. Hydrothermal mineralization in the Red Sea. In: Handbook of Marine Mineral Deposits. Routledge, London, pp. 369–395.

Shields-Zhou, G.A., Hill, A.C., MacGabhann, B.A., 2012. The Cryogenian Period. In: Gradstein, F.M., Ogg, J.G., Schmitz, M., Ogg, G. (Eds.), The Geologic Time Scale. Elsevier, Amsterdam, pp. 393–411.

Slater, B.J., Bohlin, M.S., 2022. Animal origins: the record from organic microfossils. Earth Sci. Rev. 232, 104107.

Slemons, L.O., Murray, J.W., Resing, J., Paul, B., Dutrieux, P., 2010. Western Pacific coastal sources of iron, manganese, and aluminum to the Equatorial Undercurrent. Global Biogeochem. Cycles 24 (3).

Song, Y., Gilleaudeau, G.J., Algeo, T.J., Over, D.J., Lyons, T.W., Anbar, A.D., Xie, S., 2021. Biomarker evidence of algal-microbial community changes linked to redox and salinity variation, Upper Devonian Chattanooga Shale (Tennessee, USA). GSA Bull. 133 (1–2), 409–424.

Stüeken, E.E., Kirsimäe, K., Lepland, A., Prave, A.R., 2023. Hydrothermal regeneration of ammonium as a basin-scale driver of primary productivity. Astrobiology 23 (2), 195–212.

Swanson-Hysell, N.L., Rose, C.V., Calmet, C.C., Halverson, G.P., Hurtgen, M.T., Maloof, A.C., 2010. Cryogenian glaciation and the onset of carbon-isotope decoupling. Science 328 (5978), 608–611.

Taitel-Goldman, N., Ezersky, V., Mogilyanski, D., 2009. High-resolution transmission electron microscopy study of Fe-Mn oxides in the hydrothermal sediments of the Red Sea deeps system. Clay Clay Miner. 57 (4), 465–475.

Tan, Z., Jia, W., Li, J., Yin, L., Wang, S., Wu, J., Song, J., 2021. Geochemistry and molybdenum isotopes of the basal Datangpo Formation: Implications for ocean-redox conditions and organic matter accumulation during the Cryogenian interglaciation. Palaeogeogr. Palaeoclimatol. Palaeoecol. 563, 110169.

Tazaki, K., 2000. Formation of banded iron-manganese structures by natural microbial communities. Clay Clay Miner. 48 (5), 511–520.

Tebo, B.M., Emerson, S., 1985. Effect of oxygen tension, Mn (II) concentration, and temperature on the microbially catalyzed Mn (II) oxidation rate in a marine fjord. Appl. Environ. Microbiol. 50 (5), 1268–1273.

Tebo, B.M., Bargar, J.R., Clement, B.G., Dick, G.J., Murray, K.L., Parker, D., Verity, R., Webb, S.M., 2004. Biogenic manganese oxides: properties and mechanisms of formation. Annu. Rev. Earth Planet. Sci. 32, 287–328.

Tebo, B.M., Clement, B.G., Dick, G.J., 2007. Biotransformations of manganese. In: Hurst, C.J., Crawford, R.L., Garland, J.L., Lipson, D.A. (Eds.), Manual of Environmental Microbiology, 3rd edn. American Society of Microbiology, pp. 1223–1238.

Tribovillard, N., Algeo, T.J., Lyons, T., Riboulleau, A., 2006. Trace metals as paleoredox and paleoproductivity proxies: an update. Chem. Geol. 232 (1–2), 12–32.

Tyler, P.A. (Ed.), 2003. Ecosystems of the Deep Oceans. Elsevier, Amsterdam, p. 569.

Urban, H., Stribrny, B., Lippolt, H.J., 1992. Iron and manganese deposits of the Urucum district, Mato Grosso do Sul. Brazil. Economic Geology 87 (5), 1375–1392.

Usui, A., Yuasa, M., Yokota, S., Nohara, M., Nishimura, A., Murakami, F., 1986. Submarine hydrothermal manganese deposits from the Ogasawara (Bonin) Arc, off the Japan Islands. Mar. Geol. 73 (3–4), 311–322.

Van Cappellen, P., Viollier, E., Roychoudhury, A., Clark, L., Ingall, E., Lowe, K., Dichristina, T., 1998. Biogeochemical cycles of manganese and iron at the oxic–anoxic transition of a stratified marine basin (Orca Basin, Gulf of Mexico). Environ. Sci. Tech. 32 (19), 2931–2939.

Vandieken, V., Pester, M., Finke, N., Hyun, J.H., Friedrich, M.W., Loy, A., Thamdrup, B., 2012. Three manganese oxide-rich marine sediments harbor similar communities of acetate-oxidizing manganese-reducing bacteria. ISME J. 6 (11), 2078–2090.

Vandieken, V., Finke, N., Thamdrup, B., 2014. Hydrogen, acetate, and lactate as electron donors for microbial manganese reduction in a manganese-rich coastal marine sediment. FEMS Microbiol. Ecol. 87 (3), 733–745.

Varentsov, I.M., 2013. Manganese Ores of Supergene Zone: Geochemistry of Formation (Vol. 8). Springer, Berlin, p. 355.

Wallace, M.W., Shuster, A., Greig, A., Planavsky, N.J., Reed, C.P., 2017. Oxygenation history of the Neoproterozoic to early Phanerozoic and the rise of land plants. Earth Planet. Sci. Lett. 466, 12–19.

Wang, P., Algeo, T.J., Zhou, Q., Yu, W., Du, Y., Qin, Y., Xu, Y., Yuan, L., Pan, W., 2019. Large accumulations of ^{34}S-enriched pyrite in a low-sulfate marine basin: The Sturtian Nanhua Basin. South China. Precambrian Research 335, 105504.

Wang, J., Li, Z.X., 2003. History of Neoproterozoic rift basins in South China: implications for Rodinia break-up. Precambr. Res. 122 (1–4), 141–158.

Wang, X., Xie, G.J., Tian, N., Dang, C.C., Cai, C., Ding, J., Liu, B., Xing, D., Ren, N., Wang, Q., 2022. Anaerobic microbial manganese oxidation and reduction: a critical review. Sci. Total Environ. 153513.

Wang, Y., Zhang, A., Fan, W., Zhao, G., Zhang, G., Zhang, Y., Zhang, F., Li, S., 2011. Kwangsian crustal anatexis within the eastern South China Block: geochemical, zircon U-Pb geochronological and Hf isotopic fingerprints from the gneissoid granites of Wugong and Wuyi-Yunkai Domains. Lithos 127 (1–2), 239–260.

Wedepohl, K. H. (1978). Manganese. In: Wedepohl, K. H. (ed.), Handbook of Geochemistry, Vol. II, Springer, Berlin, pp. 25-B to 25-O.

Wei, W., Algeo, T.J., 2020. Elemental proxies for paleosalinity analysis of ancient shales and mudrocks. Geochim. Cosmochim. Acta 287, 341–366.

Wei, W., Algeo, T.J., Lu, Y., Lu, Y.C., Liu, H., Zhang, S., Peng, L., Zhang, J., Chen, L., 2018. Identifying marine incursions into the Paleogene Bohai Bay Basin lake system in northeastern China. Int. J. Coal Geol. 200, 1–17.

Wei, G.Y., Wei, W., Wang, D., Li, T., Yang, X., Shields, G.A., Zhang, F., Li, G., Chen, T., Yang, T., Ling, H.F., 2020. Enhanced chemical weathering triggered an expansion of euxinic seawater in the aftermath of the Sturtian glaciation. Earth Planet. Sci. Lett. 539, 116244.

Wei, W., Yu, W., Algeo, T.J., Herrmann, A.D., Zhou, L., Liu, J., Wang, Q., Du, Y., 2022. Boron proxies record paleosalinity variation in the North American Midcontinent Sea in response to Carboniferous glacio-eustasy. Geology 50 (5), 537–541.

White, W.M., 2023. Isotope Geochemistry. John Wiley & Sons, New York, p. 708.

Wilson, J.T., 1963. Hypothesis of earth's behaviour. Nature 198 (4884), 925–929.

Wittkop, C., Swanner, E.D., Grengs, A., Lambrecht, N., Fakhraee, M., Myrbo, A., Bray, A., Poulton, S., Katsev, S., 2020. Evaluating a primary carbonate pathway for manganese enrichments in reducing environments. Earth Planet. Sci. Lett. 538, 116201.

Wu, C., Zhang, Z., Xiao, J., Fu, Y., Shao, S., Zheng, C., Yao, J., Xiao, C., 2016. Nanhuan manganese deposits within restricted basins of the southeastern Yangtze Platform, China: Constraints from geological and geochemical evidence. Ore Geol. Rev. 75, 76–99.

Xiao, J., He, J., Yang, H., Wu, C., 2017. Comparison between Datangpo-type manganese ores and modern marine ferromanganese oxyhydroxide precipitates based on rare earth elements. Ore Geol. Rev. 89, 290–308.

Xu, L., Frank, A.B., Lehmann, B., Zhu, J., Mao, J., Ju, Y., Frei, R., 2019. Subtle Cr isotope signals track the variably anoxic Cryogenian interglacial period with voluminous manganese accumulation and decrease in biodiversity. Sci. Rep. 9 (1), 1–8.

Yan, H., Pi, D.H., Jiang, S.Y., Mao, J., Xu, L., Yang, X., Hao, W., Mänd, K., Li, L., Konhauser, K.O., Robbins, L.J., 2022. Mineral paragenesis in Paleozoic manganese ore deposits: Depositional versus post-depositional formation processes. Geochim. Cosmochim. Acta 325, 65–86.

Yao, W.H., Li, Z.X., Li, W.X., Li, X.H., Yang, J.H., 2014. From Rodinia to Gondwanaland: A tale of detrital zircon provenance analyses from the southern Nanhua Basin. South China. American Journal of Science 314 (1), 278–313.

Yonkee, W.A., Dehler, C.D., Link, P.K., Balgord, E.A., Keeley, J.A., Hayes, D.S., Wells, M. L., Fanning, C.M., Johnston, S.M., 2014. Tectono-stratigraphic framework of Neoproterozoic to Cambrian strata, west-central US: Protracted rifting, glaciation, and evolution of the North American Cordilleran margin. Earth Sci. Rev. 136, 59–95.

Yu, W., Algeo, T.J., Du, Y., Maynard, J.B., Guo, H., Zhou, Q., Peng, T., Wang, P., Yuan, L., 2016. Genesis of Cryogenian Datangpo manganese deposit: Hydrothermal influence and episodic post-glacial ventilation of Nanhua Basin, South China. Palaeogeogr. Palaeoclimatol. Palaeoecol. 459, 321–337.

Yu, W., Algeo, T.J., Zhou, Q., Du, Y., Wang, P., 2020. Cryogenian cap carbonate models: A review and critical assessment. Palaeogeogr. Palaeoclimatol. Palaeoecol. 552, 109727.

Yu, W., Algeo, T.J., Zhou, Q., Wei, W., Yang, M., Li, F., Du, Y., Yuan, L., Pan, W., Wang, P., 2022. Evaluation of alkalinity sources to Cryogenian cap carbonates, and implications for cap carbonate formation models. Global Planet. Change 217, 103949.

Yu, H., Leadbetter, J.R., 2020. Bacterial chemolithoautotrophy via manganese oxidation. Nature 583 (7816), 453–458.

Yu, W., Polgári, M., Gyollai, I., Fintor, K., Szabó, M., Kovács, I., Fekete, J., Du, Y., Zhou, Q., 2019. Microbial metallogenesis of Cryogenian manganese ore deposits in South China. Precambr. Res. 322, 122–135.

Zhang, S., Jiang, G., Han, Y., 2008. The age of the Nantuo Formation and Nantuo glaciation in South China. Terra Nova 20, 289–294.

Zhang, F.F., Zhu, X.K., Yan, B., Kendall, B., Peng, X., Li, J., Algeo, T.J., Romaniello, S., 2015. Oxygenation of a Cryogenian ocean (Nanhua Basin, South China) revealed by pyrite Fe isotope compositions. Earth Planet. Sci. Lett. 429, 11–19.

Zhou, Q., Du, Y. S., & Qin, Y. (2013). Ancient natural gas seepage sedimentary-type manganese metallogenic system and ore-forming model: A case study of 'Datangpo type' manganese deposits formed in rift basin of Nanhua Period along Guizhou-Hunan-Chongqing border area. Mineral Deposits, 032.003(2013), 457-466 (in Chinese with English abstract).

Zhou, C., Tucker, R., Xiao, S., Peng, Z., Yuan, X., Chen, Z., 2004. New constraints on the ages of Neoproterozoic glaciations in South China. Geology 32, 437–440.

Zhou, Z., Wen, H., Qin, C., de Fourestier, J., Liu, L., Shi, Q., 2018. The genesis of the Dahebian Zn-Pb deposit and associated barite mineralization: Implications for hydrothermal fluid venting events along the Nanhua Basin, South China. Ore Geol. Rev. 101, 785–802.

Zhou, Q., Wu, C., Hu, X., Yang, B., Zhang, X., Du, Y., Xu, K., Yuan, L., Ni, J., Hu, D., Zhang, S., Shen, X., Liu, Y., Xie, X., Wang, J., 2022. A new metallogenic model for the giant manganese deposits in northeastern Guizhou. China. Ore Geology Reviews 149, 105070.